RBS INVESTIGATION OF THE DIFFUSION OF IMPLANTED XENON IN 6H-SIC

BY

THABSILE THEODORA THABETHE

Submitted in partial fulfilment of the requirements for the

degree of

MAGISTER SCIENTIAE

In the Faculty of Natural and Agricultural Sciences at University

of Pretoria

November 2013

Supervisor/Promoter: Prof J.B. Malherbe

Co-Supervisor: T.T. Hlatshwayo

DECLARATION

I, Thabsile Theodora Thabethe, declare that the dissertation, which I hereby submit for the degree of MSc in University of Pretoria, is my own work and has not been submitted by for a degree at this or any other tertiary institution.

Signature: ……………………….

Date: ………………………….

RBS INVESTIGATION OF THE DIFFUSION OF IMPLANTED XENON IN 6H-SIC

BY

T.T. Thabethe

Supervisor: J.B. Malherbe

Co-Supervisor: T.T. Hlatshwayo

In modern high temperature nuclear reactors, silicon carbide (SiC) is used as the main diffusion barrier for the fission products in coated fuel spheres called TRISO particles. In the TRISO particle, pyrolytic carbon and SiC layers retain most of the important fission products like xenon, krypton and cesium effectively at temperatures up to 1000 ^{o}C. Previous studies have shown that 400 ^{o}C to 600 ^{o}C implantation of heavy ions into single crystal 6H-SiC causes the SiC to remain crystalline with many point defects and dislocation loops (damage). The release of Xe at annealing temperatures above 1400 ^{o}C is governed by the normal volume diffusion without any hindrance of trapping effects.

In this study two phenomena in single crystal 6H-SiC implanted by 360 keV Xenon ions were studied using Rutherford Backscattering Spectroscopy (RBS) and channeling. Radiation damage and its annealing behavior at annealing temperatures ranging from 1000 ^{o}C to 1500 ^{o}C, and the diffusion of xenon in 6H-SiC at these annealing temperatures were investigated.

360keV xenon ions were implanted into a single crystalline wafer (6H-SiC) at 600 ^{o}C with a fluence of 1×10^{16} cm^{-2}. The sample was vacuum annealed in a computer control Webb 77 graphite furnace. Depth profiles were obtained by Rutherford backscattering spectrometry (RBS). The same set-up was used to investigate radiation damage of the 6H-SiC sample by channeling spectroscopy.

Isochronal annealing was performed at temperatures ranging from 1000 to 1500 °C in steps of 100 ^{o}C for 5 hours. Channeling revealed that the 6H-SiC sample retained most of its crystal structure when xenon was implanted at 600 °C. Annealing of the

radiation damage took place when the sample was heat treated at temperatures ranging from 1000 ^{o}C to 1500 ^{o}C. The damage peak almost disappears at 1500 ^{o}C but the virgin spectrum was not achieved. This happened because of dechanneling due to extended defects like dislocations remaining in the implanted region. RBS profiles showed that no diffusion of the Xe occurred when the sample was annealed at temperatures from 1000 ^{o}C to 1400 ^{o}C. A slight shift of the xenon peak position towards the surface after annealing at 1400 °C was observed for 600 ^{o}C implantation. After annealing at 1500° C, a shift toward the surface accompanied by a broadening of the Xe peak indicating that diffusion took place. This diffusion was not accompanied by a loss of xenon from the SiC surface. The shift towards the surface is due to thermal etching of the SiC at 1400-1500 °C.

Modern high temperature gas-cooled reactors operate at temperatures above 600 ^{o}C in the range of 750 ^{o}C to 950 ^{o}C. Consequently, our results indicate that the volume diffusion of Xenon in SiC is not significant in SiC coated fuel particles.

Acknowledgements

I will like to acknowledge the following people for their support and valuable contribution in the success of my study.

- ➢ My academic promoter, Prof. J.B. Malherbe, my co-promoter Dr. T.T. Hlatswayo, Prof. E. Friedland and Prof. C.C. Theron for their guidance, support, discussion during the course of this study.

- ➢ The heard of department, Prof. C.C Theron , for arranging some part-time work in the department, which helped me financially during this study.

- ➢ Mr. J. Smith, Dr. T.T. Hlatswayo and Mr. R.D. Kuhudzai, for all their help they provided with the accelerator.

- ➢ NRF, for providing me with a bursary that enabled my studies.

- ➢ My friend Tshepiso Pila, for the love and support.

- ➢ Fellow students in the Physics department, Chemist Mabena, Opeyemi Saint, Eric Njoroge, Cecil Ouma, Joseph Kuhudzai, FredJoe Nambala and Prime Niyongabo for all their help, encouragement and moral support.

- ➢ My family, mostly my mother, grandmother, siblings and Ephraim Shongwe, for their endless love, support and encouragements throughout my studies and life.

- ➢ Lastly God Almighty for giving me strength.

TABLE OF CONTENTS

CHAPTER 1

INTRODUCTION

1.1 High Temperature Gas-cooled Reactors (HTGR)

With the decreasing fossil fuel supply, the problem of emission of greenhouse gas and increasing energy demand, alternative (to the nearly ubiquitous fossil fuel power plants) ways of energy supply has to be introduced. One alternative is the High Temperature Gas-cooled Nuclear Reactor (HTGR), which is one of the most promising future energy supplier around the world. High temperature gas-cooled reactors can be used for thermo-chemical processes to produce hydrogen from water as an energy carrier [www1] and for generating electricity. Safety is one of the important factors with HTGR. Safety can be achieved by retaining the radioactive fission products (FPs) inside the fuel elements. The generators use helium as a coolant and transfers energy absorbed in the core to a secondary loop through a special heat exchange, where steam is generated [www2].

The HTGR uses fuel particles, which are encapsulated by chemical vapour deposited (CVD) layers. These layers serve as the barrier to prevent FPs release. The recent reactors designs use fuel kernels (UO_2) surrounded by four successive layers, namely low-density pyrolytic carbon buffer, inner high-density pyrolytic carbon (IPyC), silicon carbide (SiC) and outer high-density pyrolytic carbon (OPyC), as shown in figure 1-1. The particle is termed the TRISO (Tri-Isotropic) particle. The fuel kernels are 0.5 mm in diameter, the buffer layer is 95 μm thick, IPyC and OPyC are each 40 μm thick and the SiC is 35μm thick. The use of silicon carbide (SiC) in the TRISO are due to their physical and chemical properties. The properties of carbon are: its stability to very high temperature, nontoxic, cheap, reasonable moderator and small neutron capture cross-section [Hla10]. SiC provides chemical and physical properties like: extreme hardness, high thermal conductivity, small neutron capture cross-sections, high temperature stability, radiation resistance, etc. [Fuk76] [Wen98] [Bus03]. The functions of low-density pyrolytic carbon buffer are to provide voids for the gaseous FPs and carbon monoxides produced, to protect the IPyC from damage by

4

reducing the fission recoils and to accommodate the deformation of the fuel kernel during burn-up. The IPyC and low-density pyrolytic carbon buffer both act as a diffusion barrier for gaseous FPs. According van der Berg et al. [Van10], the laminar structures of the carbon sphere in both the buffer and IPyC layers also have stress and gas storage function. The SiC layer acts as the main barrier for solid FPs release. The OPyC mechanically protects SiC. In the pebble bed modular reactor (PBMR) the fuel particles are mixed with graphite to form a fuel spheres called pebbles.

The use of the HTGR will be determined by their ability to retain radioactive FPs. These FPs are dangerous when exposed to the environment and may lead to death. Inhalation, ingestion and absorption are the main possible ways of exposure to radiation. The retention of these radioactive FPs is also important for the people working with nuclear reactors so that they do not get exposed to FPs during refuelling and servicing. According to Friedland et al. [Fri11], the TRISO fuel particles retain most of the important FPs like cesium, iodine, silver and strontium quite effectively up to 1000° C temperatures.

FUEL ELEMENT DESIGN FOR PBMR

Dia. 60mm
Fuel Sphere

5mm Graphite layer

Coated particles imbedded in Graphite Matrix

Section

Pyrolytic Carbon 40/1000mm
Silicon Carbide Barrier Coating 35/1000mm
Inner Pyrolytic Carbon 40/1000mm
Porous Carbon Buffer 95/1000mm

Dia. 0,92mm
TRISO
Coated Particle

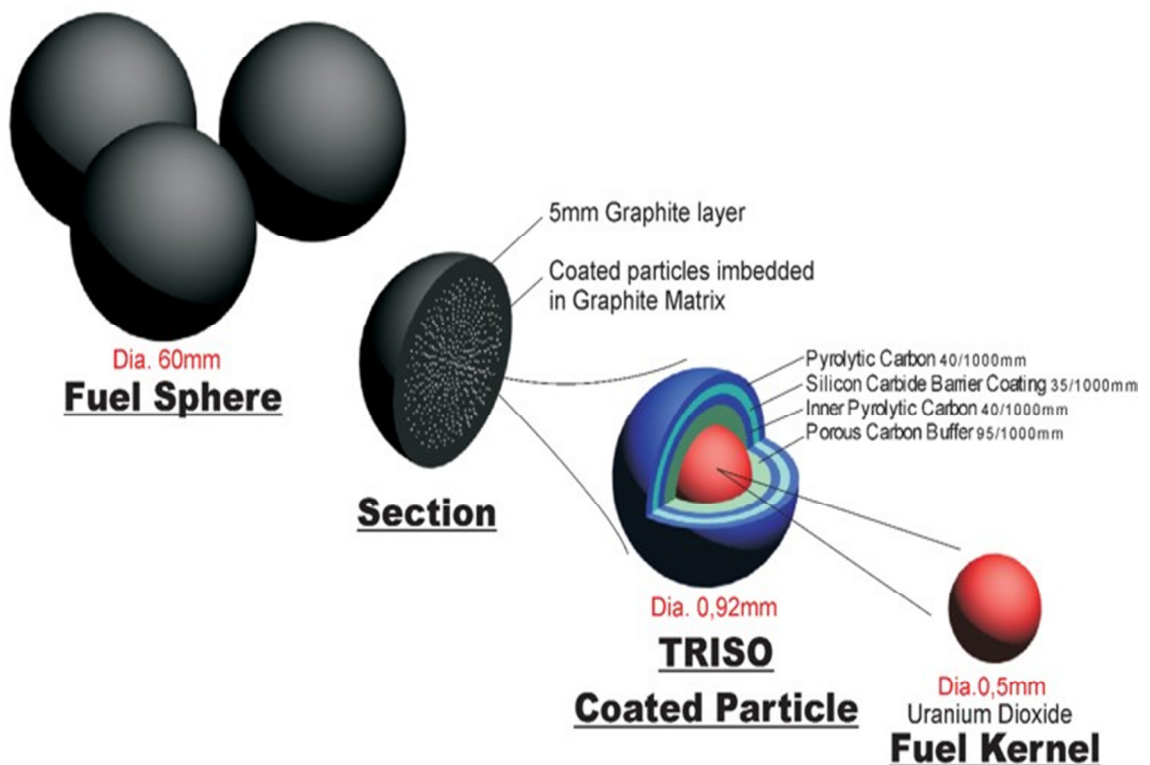Dia. 0,5mm
Uranium Dioxide
Fuel Kernel

Figure 1-1: The schematic diagram of the fuel for a Pebble Bed Modular Reactor (PBMR) and the HTR pebble cross-section [www2].

In this dissertation the diffusion of xenon implanted into 6H-SiC at 600° C and annealing of the radiation damage were investigated for the temperatures ranging from 1000° C to 1500° C in steps of 100° C. The implantation temperature of 600° C was used to approximately simulate reactor conditions. The Rutherford backscattering spectrometry (RBS) and Rutherford backscattering spectroscopy in channeling mode (RBS-C) techniques for analysis were used.
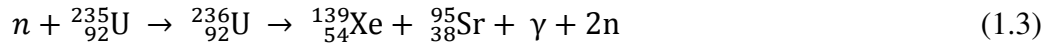
1.2   Xenon Radiological significance

This study focuses on the diffusion behavior xenon in 6H-SiC. Xenon is a common FP with most of the isotopes emanating from the fission reaction being radioactive. These radioactive isotopes of xenon are known to cause cancer. If this decaying xenon gas bombards human body with powerful gamma and beta particles it can cause cancer [www4]. It targets the lung, bones and fatty tissue [www5]. Xenon is known to have 40 unstable isotopes which have been studied [www4]. ^{131m}Xe, ^{133}Xe, ^{135}Xe, are FPs from ^{235}U and ^{239}P and are used as indicators for nuclear explosions [www4].

^{136}Xe is known to be the longest lived isotope; it double beta-decays with a half-life of 2×10^{21} years with the next long lived isotope ^{127}Xe with a half-life of 36.345 days. Xe is produced by neutron capture of other FPs in nuclear reactors and the Xe isotopes also by neutron emission to form other FPs. ^{135}Xe has a half-life of 9.1h and a large neutron absorption cross section, while ^{133}Xe isotope has a half-life of 5.3 days. ^{133}Xe and ^{135}Xe isotopes decay to form ^{133}Cs and ^{135}Cs plus a neutron. ^{135}Xe acts as a neutron absorber or poison and interrupts the fission chain reaction [Ima09]. Iodine (^{135}I) with a half-life of 6.57 h produces ^{135}Xe from decaying. It undergoes beta decay to form ^{135}Xe.

$$^{135}_{53}\text{I} \ \rightarrow \ ^{135}_{54}\text{Xe} + \ \beta^{-} \tag{1.1}$$

$$^{135}_{54}\text{Xe} \ \rightarrow \ ^{135}_{55}\text{Cs} + \ \beta^{-} + \ \gamma \tag{1.2}$$

The decay of ^{135}Xe forms cesium (^{135}Cs). Most of the ^{135}Xe yield comes from the decay of ^{135}I (around 95%), while only 6.3% fission of ^{135}Xe is from uranium [www6]. Again Xenon isotopes can be produced from the following possible fission reaction:

$$n + {}^{235}_{92}\text{U} \rightarrow {}^{236}_{92}\text{U} \rightarrow {}^{139}_{54}\text{Xe} + {}^{95}_{38}\text{Sr} + \gamma + 2\text{n} \qquad (1.3)$$

where ^{235}U absorbs the neutron to form an unstable $^{236}_{92}$U which survives for about 10^{-14} s, and then fission occurs. The fission reaction splits to form two fragments, releases two neutrons and gamma rays. The two fragments formed in (1.3) are the isotopes $^{139}_{54}$Xe of xenon and $^{95}_{38}$Sr of strontium.

1.3 Silicon Carbide (SiC)

SiC is used in nuclear environments based on its properties mentioned in section 1.1. SiC has a Mohs hardness of 9.5 making it the second hardest naturally occurring material known; only diamond is harder with a Mohs hardness of 10. In SiC the short bond length of 1.89Å between Si and C atoms results in excellent hardness and high bond strength [Zso05] [www3]. SiC is a good abrasive with high corrosion resistance. Its high thermal conductivity allows for high operating fuel temperatures. It also has good dimensional stability (i.e. its ability to be able to maintain or keep its shape over a long period of time, and also under specific conditions) under neutron radiation. SiC sublimes at a temperature around 2800 $^{\text{o}}$C and also it has been noted that it starts to decompose at temperatures above 1600 $^{\text{o}}$C [Cor08][Hla12][Shi06]. Because of its good properties such as its stability to very high temperatures, SiC is thus used as the main barrier for fission products in TRISO particles. The temperature at which most of the HTGR operate is around 950 $^{\text{o}}$C [Saw00] [Ver12]. According to Kuhudzai [Kuh10], under normal operation conditions of the reactor, SiC should be a reliable diffusion barrier for FPs.

SiC is a binary compound with the same number of Si and C atoms. The structural unit of SiC is considered to be covalently bonded, with an ionic contribution of 12%, due to the difference in electronegativity (Si positively charged, C negatively

7

charged) , making the Si and C bond nearly pure covalent. The basic structural units
of SiC are a tetrahedron, and can be either SiC_4 or CSi_4 as shown in figure 1-2.
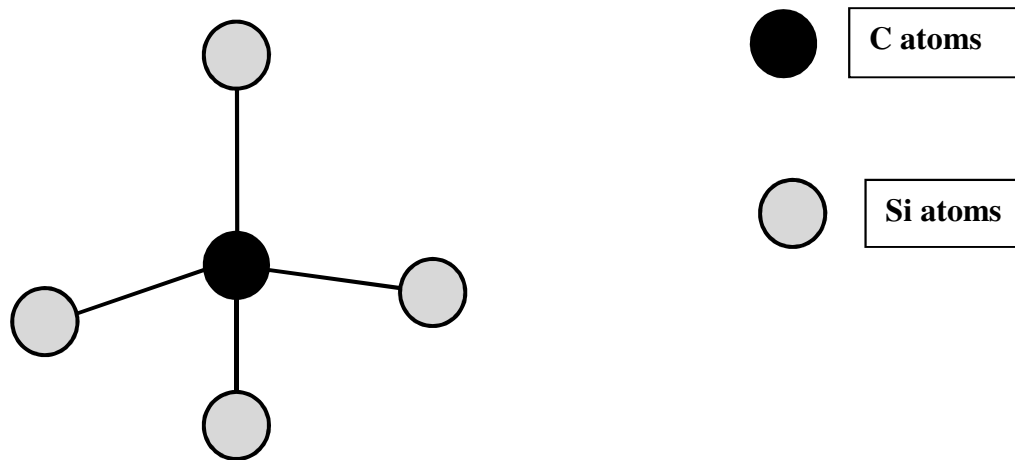

Figure 1-2: Tetrahedral Silicon Carbide structure.

 SiC has different polytypes, they come about because of the different stacking
sequence of the identical atomic planes (close-packed hexagonal layers). SiC has
more than 200 polytypes which have been identified [Zso05][Dev00]. To describe the
different polytypes the following notation (the Ramsdell notation) is used: The cubic
zinc blende SiC structure is used as the basis where the first layer is named A and the
second is named B and the other C (they are placed according to a close-packed
structure) as shown in figure 1-3. In the Ramsdell notation the number of layers in the
stacking direction, before repeating the sequence, is combined with the letter
representing the Bravais lattice type: cubic (C), hexagonal (H) or rhombohedral (R)
[www2]. The following common hexagonal and cubic polytypes and their stacking

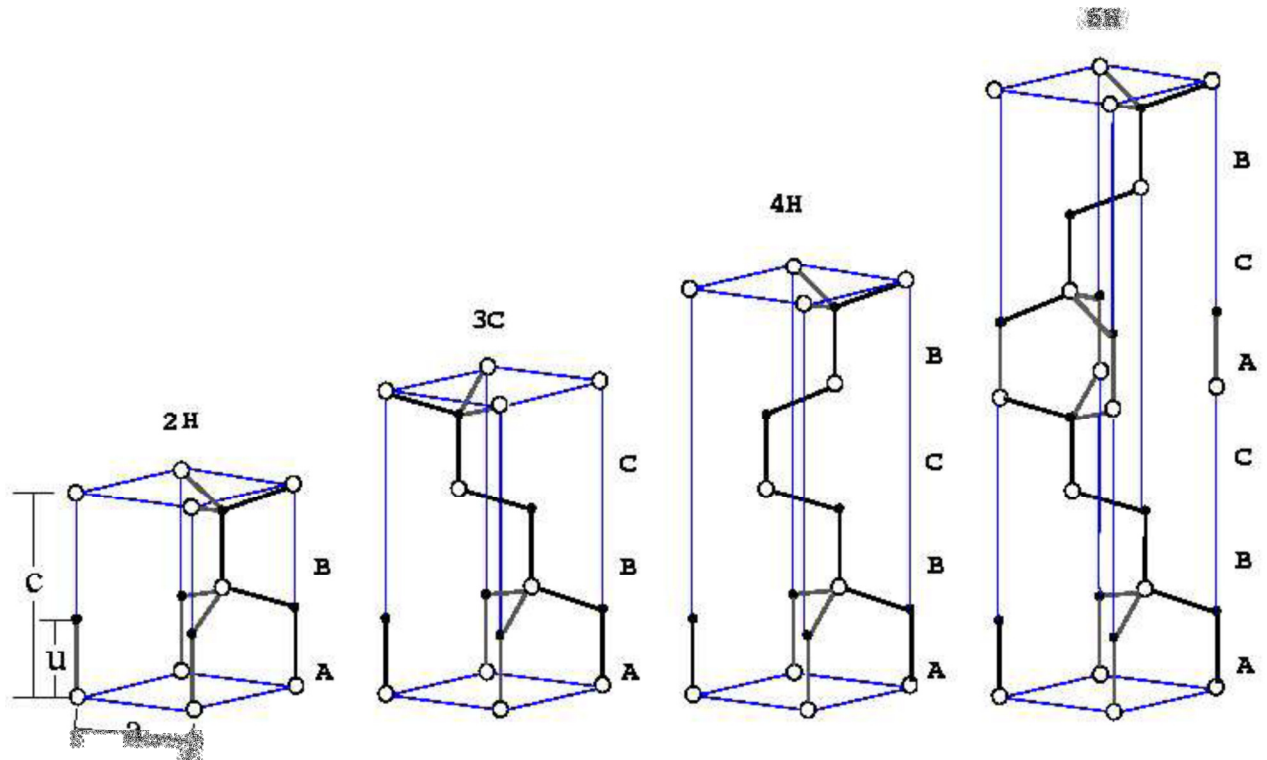sequence are shown in figure 1-3, 2H-SiC, 3C-SiC, 4H-SiC and 6H-SiC, with 3C-SiC being the cubic polytype.

Figure 1-3: A schematic representation showing the common SiC polytypes and their stacking sequence [www3].

1.4 Radiation Damage in SiC

To study the effectiveness of SiC in retaining FPs, xenon ion (as a FPs) was implanted into SiC and the production of radiation damage and diffusion behavior of xenon were analyzed. This was done by analyzing the radiation damage and diffusion behavior of xenon using Rutherford backscattering spectroscopy and Channeling. In several studies it has been reported that implanting at temperatures around 300 to 625 °C, SiC remains crystalline with many point defects and dislocation loops (damage)

9

[FuK76][Hla12]. Studies by Fukuda et al. [FuK76] reveal that at implantation temperatures of 400 to 625 °C, β-SiC remained crystalline with many point defects and dislocation loops (damage) after a thermal neutron dose of 8.4×10^{16} n.cm^{-1} and a fast neutron dose of 1.5×10^{15} n.cm^{-1}. Zolnai et al [Zol02] implanted 200keV Al$^+$ at different fluences ranging from 3.5×10^{13} to 2.8×10^{14} ions/cm^{-2} at room temperature. They observed that relatively low damage was formed in 6H-SiC at these implantations and they also found that the C/Si damage ratio decreased with an increase in fluence.

Wesch et al [Wes95] implanted 230 keV Ga$^+$ and 300keV Sb$^+$ at different temperatures and fluences. Their study showed that 6H-SiC became amorphous near the surface for room temperature (27 ^{o}C) and 200 ^{o}C implantations with fluences between 2×10^{14} to 5×10^{14} cm^{-2}. They also noticed that implanting with a fluence of 1×10^{16} cm^{-2} at a temperature around 300 ^{o}C and above avoid amorphization of SiC. Thus implantation at higher temperature for fluences above 1×10^{16} cm^{-2} is required to avoid amorphization.

According to Bus et al. [Bus03], the recrystallization of SiC damage upon annealing depends on both the amount of damage created during implantation as well as the annealing temperature. McHargue et al. [McH93] found that the annealing of highly damaged (amorphous) SiC resulted in recrystallization at temperatures ranging from 750 to 1700 ^{o}C. When the damage is less (that is the implanted region remains crystalline after implantation with damage formed), it anneals in one stage in the temperatures range of 200 to 1000 ^{o}C. Wendler et al. [Wen98] reported that implantation of 300 keV Sb$^+$ into 6H-SiC at room temperature with a fluence of 3×10^{14} cm^2 caused the SiC to become amorphous. The results showed that when annealed at temperatures above 950 ^{o}C, crystallization was found which resulted in a highly defected crystalline structure. Perfect recrystallization was also reported after annealing at temperature of 1500 ^{o}C for 60 minutes in argon ambient and the implanted ion could no longer be detected, indicating that the amorphous layer was etched away.

Hlatshwayo et al. [Hla12], implanted (360 keV) Ag^+ into 6H-SiC at 350 and 600 ^oC with a fluence of 2×10^{16} cm^{-2}. Defects were created on the SiC structure although it maintained its crystalline form. They observed that isothermal annealing at 1500 ^oC for 30min, 3h and 6h at 600 ^oC implantation caused removal of defects with retention of some defects. Fukuda et al. [Fuk76] briefly mentioned that for β-SiC implanted with Xe^+ that after annealing above 1600 ^oC a small amount of disorder still survived. His main discussion was on the diffusion of xenon in SiC.

1.5 Diffusion Behavior of Xenon

A single publication with regard to diffusion behavior of Xenon in SiC has been published. Fukuda et al. [Fuk76] investigated Xenon diffusion behavior in pyrolytic SiC. They used β-SiC, which was crushed to powder and dipped in aqueous uranyl nitrite. Then dried and irradiated at ambient temperature to a thermal neutron dose of 8.4×10^{16} n.cm^{-1} and fast neutron dose of 1.5×10^{15} n.cm^{-1} to produce ^{133}Xe-recoiled SiC. These samples where then left for 7 days to allow ^{133}I to decay and form ^{133}Xe. Isochronal and isothermal annealing methods (under He gas flow) were done on the samples. The γ-ray spectrometry analysis was used to measure the release of xenon during annealing and remaining xenon after annealing to be able to obtain the fractional release.

The fraction of release versus temperature and fraction of release versus square root of time graph was plotted. Finally the release rate at different temperatures and time were compared. From the graphs the release of xenon from the pyrolytic SiC was noticed to be taking place at different annealing temperatures. They concluded from their experiment that the release of Xe at annealing temperatures below 1200 ^oC (release for temperatures around 600 ^oC) might due to interstitial diffusion coupled with the ejection of ^{133}Xe trapped in the defects. At temperatures ranging from 1200 ^oC to 1400 ^oC, grain boundary diffusion was the dominant mechanism, while above 1400 ^oC the release is governed by the normal volume diffusion without any hindrance of trapping effects.

1.6   The Dissertation outlay

In this study the diffusion behavior of xenon implanted in 6H-SiC together with annealing of radiation damage retained after implantation were investigated using RBS and RBS-C. 360keV Xe was implanted at 600 ^{o}C with a fluence of 1×10^{16} cm^{-2}. The investigation was done using annealing temperatures ranging from 1000 to 1500 ^{o}C in step of 100 °C.

In chapter 2 diffusion theory is discussed, chapter 3 provides a brief description of ion implantation, in chapter 4 Rutherford Backscattering Spectroscopy (RBS) is discussed, chapter 5 is the experimental procedure in details, chapter 6 presents and discusses the results and chapter 7 summarizes and concludes on the results.

1.7   References

[Bus03] T. Bus, A. van Veen, A. Shiryaev, A.V. Fedorov, H. Schut, F.D. Tichelaar and J. Sietsma. Mater. Sci. Eng. B 102 (2003) 269.

[Cor08] E. L. Corral, Adva. Mater. Proce, 166 (2008) 30.

[Dev00] R. Devanathan and W. Weber, Nucl. Mater.278 (2000) 258

[Fri11]   E. Friedland, N.G. van der Berg, J.B. Malherbe, J.J Hancke, J. Barry, E. Wendler and W. Wesch, J. Nucl. Mater. 410 (2011) 24

[Fuk76] K. Fukuda and K. Iwamoto, J. Mater. Sci. 11 (1976) 522.

[Han03] D. Hanson, "A Review of Radionuclide Release From HTGR Cores during Normal Operation", EPRI, Palo Alto, CA (2003) 1009382.

[Hla12] T.T. Hlatshwayo, J.B. Malherbe, N.G. van der Berg, A,J. Botha and P. Chakraborty, Nucl. Instr. Meth. B 273 (2012) 61.

[Hla10] T. T. Hlatshwayo," Diffusion of silver in 6H-SiC", PhD Thesis, Department of Physics, University of Pretoria, (2010).

[Ima09] T. Imanaka and N. Kawano, Hiroshima Peace Science 31 (2009) 65.

[Kuh10] R. J. Kuhudzai, "Diffusion of ion implanted iodine in 6H-SiC", MSc dissertation, Department of Physics, University of Pretoria, (2010).

[McH93] C. J. McHargue, and J.M. Williams, Nucl. Instr. Meth. B80/81 (1993) 889

[Saw00] K. Sawa, S. Ueta and T. Iyoku, "Research and development program of HTGR fuel in Japan", Nuclear Science and Engineering Department, Japan Atomic Energy Agency, Japan, (2000), p.208

[Shi06] K. Shimoda, N. Eiza, J. Park, T. Hinoki, A. Kohyama and S. Kondo, Mat. Trans. 47 (2006) 1204.

[Van10] N. G. van der Berg, J. B. Malherbe, A. J. Botha and E. Friedland, Surf. Interface Anal. 42 (2010) 1156.

[Ver12] K. Verfondern, "HTGR fuel overview",IEK-6, Research Center Jülich, Germany IAEA Training Course on HTGR Technologie, Beijing, China, 22-26 October 2012. Slide.10

[Wen98] E. Wendler , A. Heft and W. Wesch, Nucl. Instr. Meth.B 141 (1998) 105

[Wes95] W. Wesch, A. Heft, J. Heindl b, H.P. Strunk, T. Bachmann, E. Glaser and E. Wendler, Nucl. Instr. Meth. B 106 (1995) 339

[www1] https://www.google.co.za/#hl=en&tbo=d&sclient=psy- , 12 December 2012

[www2] www.pbmr.co.za,12 December 2012

[www3]   http://areeweb.polito.it/ricerca/micronanotech/Papers/thesis-carlo.pdf.12 December 2012.

 [www4] http://agreenroad.blogspot.com/2012/10/radioactive-xenon-gas-dangerous-and.html#!/2012/10/radioactive-xenon-gas-dangerous-and.html,   12 December 2012.

[www5] www.**lantheus**.com/PDF/msds/**XenonLantheus**Complete.PDF,20   June 2012

[www6] http://en.wikipedia.org/wiki/Iodine_pit,12 December 2012.

 [Zol02] Z. Zolnai , N.Q. Khánh , E. Szilágyi , E. Kótai, A. Ster, M. Posselt, T. Lohner and J. Gyulai, Diam. Relat. Mater 11 (2002) 1239.

[Zso05] Z. Zolnai, "Irradiation- induced crystal defects in silicon carbide", PhD Thesis,Department of Atomic Physics, Budapest University of Technology and Economics, (2005).

CHAPTER 2

DIFFUSION

In solid materials atoms are always oscillating about their lattice sites. For an atom to be able to change lattice site, it requires enough potential energy to overcome the barrier between itself and neighboring atom. Thus the process by which matter is transported from a region of high concentration to a region of low concentration in the same material as a result of random motion is called diffusion [Cra75]. The net flux results from the random jump of atoms from a region of high concentration to a region of low concentration. Diffusion transport thus depends on the concentration gradient of the material.

2.1   Diffusion Mechanisms

For diffusion to take place an atom must contain sufficient energy to be able to break the bonds with its neighbors and there must be an empty site. In a crystal these empty sites which enhance diffusion are defects such as vacancies and interstitial point defects. An understanding of the diffusion mechanism is of great importance, because it helps us understand the physical changes and behavior of the materials. In this section the two major diffusion mechanisms, which are vacancy and interstitial mechanisms, are discussed.

2.1.1 Vacancy Mechanism

All crystals have unoccupied lattice sites (Frenkel defect) which are called vacancies [Cal07] playing a role in the diffusion of impurities and its lattice atoms. Atom in a crystal will interchange position with the vacancy (empty space), leaving a vacancy behind. The direction of movement of atoms is opposite to that of the vacancies. This action is called vacancy diffusion. A schematic diagram illustrating the vacancy mechanism is shown below in figure 2-1.
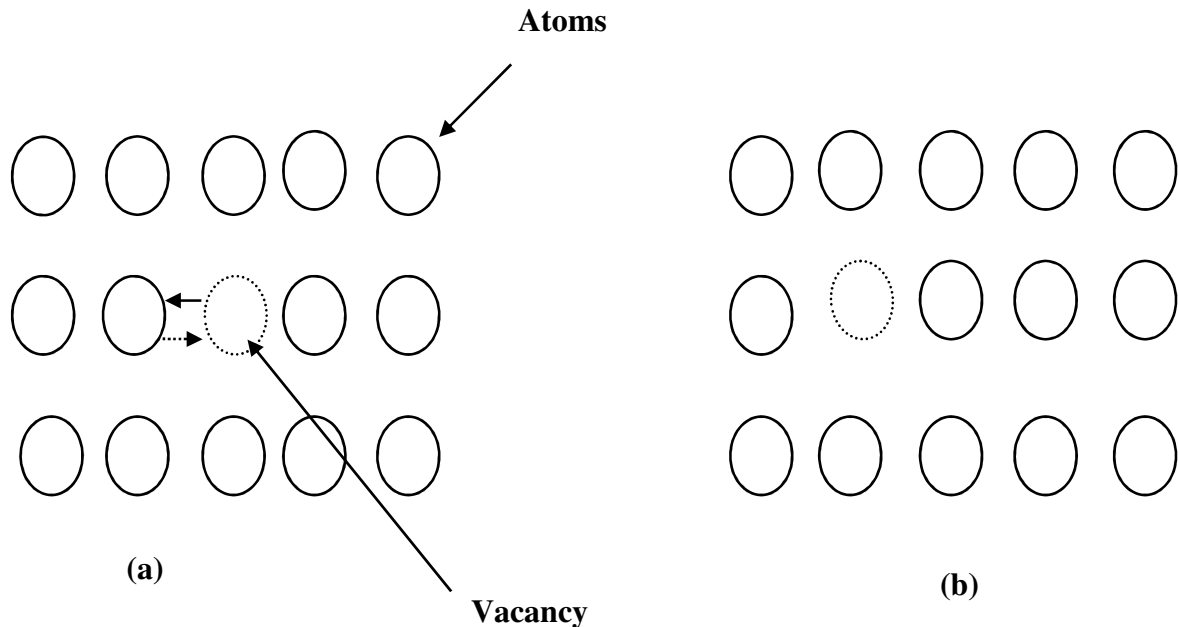
Atoms

(a)

(b)

Vacancy

Figure 2-1: Schematic representation of the vacancy diffusion mechanism, with (a) and (b) representing the position of the vacancy before and after diffusion.

2.1.2 Interstitial Mechanism

Atoms located between other atoms and not on their regular sites in crystalline materials are called interstitials. An interstitial atom may be either bigger or smaller than the host atoms. In general there are many more interstitial sites than vacancy sites thus interstitial diffusion is more likely to take place than vacancy diffusion. In metal alloys, interstitial diffusion is faster than vacancy diffusion for small interstitial atoms, because interstitials atoms are smaller and thus more mobile [Cal07]. Interstitial diffusion occurs when an interstitial atom jumps from its interstitial site to the neighboring one that is empty as shown in figure 2-2. A related diffusion mechanism called interstitialcy mechanism [She89] and is shown in figure 2-3. In this case the interstitial atom having approximately the same size as the host atoms, occupies the substitutional position of a host atom which in turn moves to an interstitial site.

16

Figure 2-2: Interstitial mechanism, (a) before and (b) after interstitial diffusion took place [Hla10].

Figure 2-3: The interstitialcy mechanism, (a) before and (b) after interstitialcy diffusion [Hla10].

2.2   The diffusion coefficient

When atoms diffuse in a particular material, they diffuse at a certain rate. The rate of diffusion of the atoms in the material is given by diffusion coefficient, D. In this dissertation we did not calculate the diffusion coefficient due the fact that diffusion was not observed in all but one concentration profile. In the future (future work) diffusion coefficient will be calculated using the Fick formalism as described below.

The flux J is used to quantify how fast diffusion occurs [Cal07]. Fick's first law relating the diffusion coefficient, D, and concentration gradient, C, to the flux, J, is

© University of Pretoria

given in equation (2.1). It describes the diffusion along a concentration gradient dC/dx [Cra75][Bar51]:

$$J = -D \frac{dC}{dx} \tag{2.1}$$

The minus sign in the equation indicates that diffusion is opposite the concentration gradient. The concentration profile and the concentration gradient changes with time, and this changes equation (2.1). The change in the concentration profile with time is described by Fick's second law. If we consider the continuity equation (i.e. 2.1)) and diffusion to be in the $+ x$ direction in equation (2.1) [Bar 51] with the diffusion coefficient, D, being independent of the position, then:

$$\frac{\partial C}{\partial t}(x,t) = \frac{\partial}{\partial x}\left(D \frac{\partial C}{\partial x}\right) = D \frac{\partial^2 C}{\partial x^2} \tag{2.2}$$

In three dimensions equation (2.2) can be written as:

$$\frac{\partial C}{\partial t} = D \nabla^2 C \tag{2.3}$$

In a limited temperature range the temperature dependence of the diffusion coefficient, follows the Arrhenius dependence [Sha73], and is written as:

$$D = D_o exp\left(\frac{-E_a}{k_B T}\right) \tag{2.4}$$

where E_a is the activation energy, D_o is the pre-exponential factor, k_B is the Boltzmann constant and T is the absolute temperature in Kelvin

2.3   Evaluation of the Diffusion coefficient

There are different methods of evaluating the diffusion of impurities in different materials, and these are discussed by Heitjans et al. [Hei05] and Crank et al. [Cra75].

In our results the depth profile is almost Gaussian, so equation (2.6) is used as the solution [Mye74]. This method assumes that the original implanted profile is purely Gaussian and gives the diffused profile as:

$$\lim_{x \to 0} \left(\frac{\partial}{\partial x} C(x,t) \right) = 0 \tag{2.5}$$

Equation (2.5) is the initial condition, for obtaining the following solution

$$C(x,t) = \left[2(\pi Dt)^{1/2} \right]^{-1} \int_0^\infty C_0(y) \times \left(e^{-\frac{(y-x)^2}{4Dt}} + e^{-\frac{(y+x)^2}{4Dt}} \right) dy \tag{2.6}$$

where $C_o(x) = C(x, 0)$ is the initial xenon profile and $C_o(x)$ is approximated to be:

$$C_o(x) = K(\pi Dt_o)^{-1/2} e^{-x^2/4Dt_o} \tag{2.7}$$

where K is an adjustable constant . After annealing for some time t the concentration profile in equation (2.6) reduces to the form:

$$C(x,t) = K[\pi Dt]^{-1/2} e^{-x^2/4Dt} \tag{2.8}$$

Now defining $W(t)$ to be the full width at half maximum (FWHM), the relationship between the final and original widths will be given by:

$$[W(t)]^2 = 4Dt\ln(2) + [W(0)]^2 \tag{2.9}$$

The slope of $[W (t)]^2$ versus the annealing time at constant temperature gives the diffusion coefficient D.

In this study, the diffusion, or more correctly the lack of diffusion, was determined by comparing the xenon depth profile before and after annealing.

2.4 References

[Bar51] R. M. Barrier, "Diffusion in and through Solids", Cambridge University Press, Cambridge, England (1951). p.1

[Cal07] D. C. William, "Materials Science and Engineering", 7th edition, John Wiley, USA (2007), p.112

[Cra75] J. Crank, "The Mathematics of Diffusion", Oxford University Press, Bristol (1975), p.2

[Hei05] P. Heitjans and J. Karger, " Diffusion in Condensed Matter", Springer, Netherlands, (2005), p.22

[Mye73] S. M. Myers, T. S. Picraux and T. S. Provender, Phys. Rev. B9/10 (1974) 3953.

[She89] P. Shewmon, " Diffusion in Solids", 2nd edition, The Mineral, Metals and Materials Society, USA (1989), p.56

[Sha73] D. Shaw, " Atomic Diffusion in Semiconductor", Plenum Press, London, (1973). p.3

CHAPTER 3

ION IMPLANTATION

Ion implantation is a technique used in introducing impurities into solids. The ions introduced into the target atoms are mediated by the kinetic energy of the ions. They collide with the host atoms leading to the ions loosing energy, and eventually coming to rest at a certain depth within the solid. This technique is mostly used as a standard doping process in SiC devices in semiconductors electronics. This chapter discusses the processes that occur during implantation.

3.1 Stopping Power

The loss of energy (E) of the ions per unit depth at a perpendicular depth x below the surface, that is dE/dx, is called the stopping power. The commonly used unit for the stopping power is eV/Å. The stopping power consists of nuclear stopping and electronic stopping. Nuclear stopping is the energy loss caused by elastic collisions between the ion and nuclei of the atoms in the target. Electronic energy loss is the energy loss caused by the interactions between the ions and the electrons of the substrate atoms [Pet03]. The sum of the two stopping power, nuclear stopping and electronic stopping can be written as the total stopping power [Hla10]:

$$S = \left(\frac{dE}{dx}\right)_n + \left(\frac{dE}{dx}\right)_e \tag{3.1}$$

The subscript n and e represent nuclear and electronic stopping powers respectively. The stopping power cross-section is defined by:

$$\varepsilon = -\frac{1}{N}\left(\frac{dE}{dx}\right) = -\frac{1}{N}\left(\frac{dE}{dx}\right)_n - \frac{1}{N}\left(\frac{dE}{dx}\right)_e = \varepsilon_n + \varepsilon_e \tag{3.2}$$

N is the atomic density, in atoms/ Å^3, ε_n and ε_e are the nuclear and electronic stopping cross sections respectively with the common unit of eV/Å. The stopping power causes the energetic ions penetrating the solid to lose energy and to eventually come to rest.

21

The independence of the nuclear and electronic stopping cross sections tells us that each of these stopping power cross sections depends on energy E of the ions as shown on figure 3-1 below:
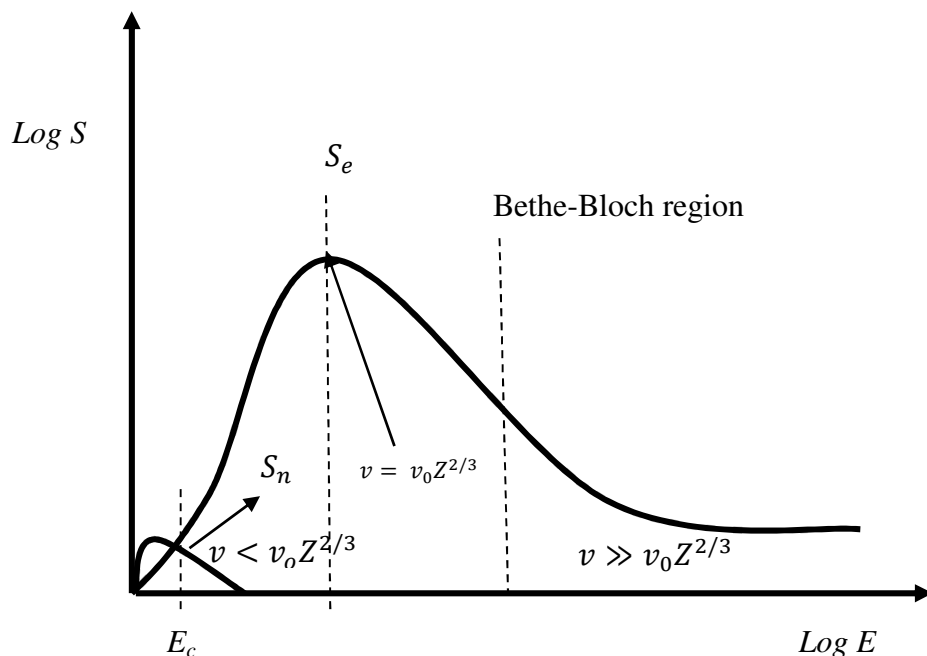

Figure 3-1: The nuclear and electronic stopping power i.e. S_n and S_e respectively. The energy regimes and symbols are discussed in the text.

From figure 3-1 it can be seen that nuclear stopping dominates at low energies while at high energies it decreases and electronic stopping dominates. Above the critical energy E_c electronic stopping starts to dominate (see figure 3-1) and after reaching a maximum, the electronic stopping cross section starts to decrease in the high energy region. The nuclear and electronic stopping power is shown in figure 3-1 is further elaborated on section 3.2 and 3.3.

3.2 Nuclear stopping

Nuclear stopping occurs when implanted ion loses its energy via elastic collision with the target atom. It dominates at low energies (figure 3-1), and the velocity v of the ion at these low energies is lower than that of critical velocity v_c of the valence electrons

[Tes95]. Elastic collision with the target nuclei dominates at these velocities and the critical velocity v_c is given by

$$v_c = v_0 Z_1^{2/3} \qquad (3.4)$$

and the Bohr velocity v_0 is given by:

$$v_0 = {e^2}/{\hbar} \qquad (3.5)$$

where Z_1 is the atomic number of the implanted ion, e is the electron charge and $\hbar$ is Planck's constant. The critical velocity, $v_{c,}$ for xenon ions is $v_c = 3.13 \times 10^9$ cm/s, and the velocity of the implanted xenon with energy 360 keV has an initial velocity of $v_i = 7.23 \times 10^7$ cm/s $\ll v_c$.

When the implanted ion collides with target atom the positively charged ions are Coulomb repelled by the positive cores of the target ion. A typical collision process is illustrated in the figure below:
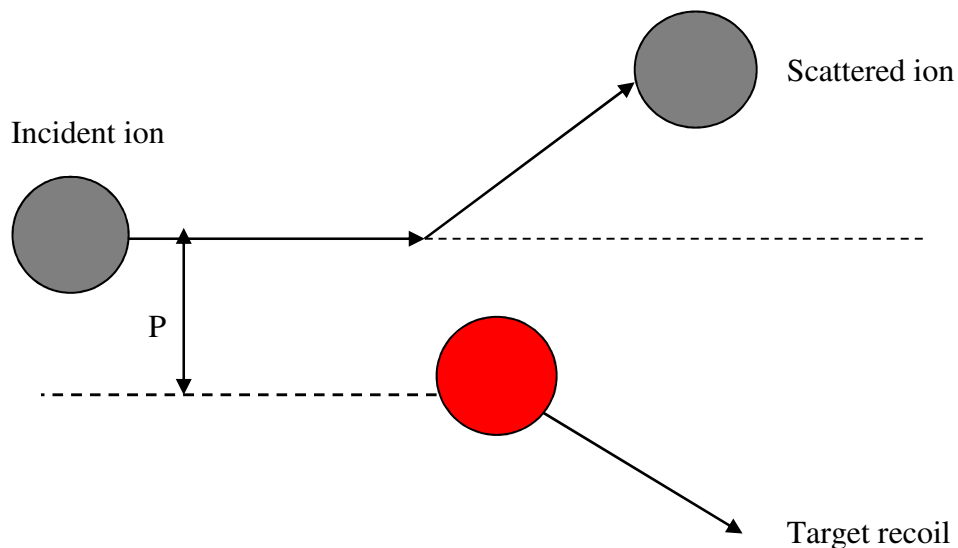

Figure 3-2: A typical schematic nuclear collision between the ion and stationary target atom.

The interatomic potential found between the charges of the ion and target atom can be written as [Zie85][www1]:

$$V = \frac{Z_1 Z_2 e^2}{4\pi\varepsilon r} \qquad (3.6)$$

where Z_1 and Z_2 are the atomic number of the implanted ions and target respectively, ε is the permittivity, e is the electronic charge and r is the interatomic distance. The

23

potential is a Coulomb potential not taking into account the screening effects. The scattering ion results in a large scattering angle and is said to be Rutherford backscattered. The perpendicular distance to the closest approach if the projectile was undeflected is called the impact parameter P.

The full effect of the positive core potential is screened from the incoming ion. To accommodate the screening the interatomic potential found between the charges of the ion and target atom is written as [Tes95]:

$$V = \frac{Z_1 Z_2 e^2}{4\pi\varepsilon r} \, \Phi\left(\frac{r}{a}\right) \tag{3.7}$$

where Φ is the screening potential and a is the screening distance. The screened Coulomb potential and the corresponding screened nuclear cross section is used to model elastic collision processes to satisfy the requirement for both small and large impact parameters. There are various screening potentials. One of the first screening potentials is the Thomas-Fermi screening potential [Zie85][www1] given by:

$$\Phi\left(\frac{r}{a}\right) = \exp\left(\frac{-r}{a}\right) \tag{3.8}$$

3.3   Electronic stopping

Electronic stopping is the process whereby incoming ions interacts inelastically with the target electrons and loses its kinetic energy to the target electrons. This depends directly on the ion's velocity and can be given in three different regions:

The first region is at low ion energies, in this region the ion velocity v is lower than $Z_1^{2/3} v_0$ and ranges from $v \approx 0.1 v_0$ to $Z_1^{2/3} v_0$ [Tes95][Zol05]. S_e at these low velocities (low energies) may be determined from the Lindhard-Scharff treatment [Lin61], which suggested that the electronic stopping power is proportional to ion velocity [Tow94]. In this region, the ion cannot transfer its energy to electrons much lower than the Fermi level [Lin63]. It only transfers its energy to electrons close to the Fermi level.

The second region the ions velocities are much greater than $Z_1^{2/3} v_0$ i.e. $v \gg Z_1^{2/3} v_0$. The ion is stripped of all its electrons, and the energy loss is proportional to Z_1^2 as shown by Bethe and Bloch (and the region is known as the Bethe-Bloch region). This region is not applicable in ion implantation.

In the intermediate region i.e. $v \approx Z_1^{2/3} v_0$, the ion becomes partially ionized and S_e reaches its maximum in this region. According to Bárdos et al. [Bár86], in this range the average charge state of the projectile depends on its energy and target material. There is no theoretical treatment for this energy region and semi empirical treatments do exist. According to Zolnai [Zol05] in this region charge exchange processes play an important role. Here, in order to model the stopping power, a so-called effective charge is introduced [Zol05].

As was shown in section 3.2, in our case the initial velocity of 360 keV xenon $v_0 \ll v_c$, indicating that the electronic stopping could be described using the Lindhard-Scharf model.

3.4   Energy loss in compounds

In targets having two or more elements, the interaction process between the ion and component target are to a first order independent. For a compound having two elements A and B, the stopping cross section for a compound A_mB_n is written as:

$$\varepsilon^{AmBn} = m\varepsilon^A + n\varepsilon^B \tag{3.9}$$

where ε^A and ε^B are the stopping power cross-sections of element A and B respectively. Equation (3.9) is known as Bragg's rule. The deviation of the energy loss from Bragg's rule is found to be 10-20% around the stopping maximum. This is because of the chemical and physical state of the medium, having an effect on the energy loss for light organic gases and for solid compounds containing heavier constituents such as oxides, nitrides, etc. [Tes95].

3.5 Energy Straggling

The statistical fluctuation in the energy loss of energetic ions after penetrating a substrate and interacting with the target atoms results in a spread in energy. This spread in energy is called energy straggling. This implies that particles having the same initial energy before penetrating the substrate of thickness Δx will have different energies after penetrating the substrate. Straggling broadens the measured energy distribution and limits the depth resolution. Bohr's theory assumed the distribution of the highly energetic ions to be Gaussian and then calculated the broadening and its variance to give [Chu78]:

$$\Omega_B^2 = 4\pi Z_1^2 Z_2 e^2 N \Delta x \qquad (3.10)$$

where Ω_B is Bohr's energy straggling, Z_1 and Z_2 are the atomic number of the ion and target atom respectively, N is the atomic density and Δx is the thickness of the target. The full width at half maximum (FWHM) of energy loss distribution is given by:

$$\text{FWHM} = 2\Omega\sqrt{2ln2} \;. \qquad (3.11)$$

where Ω is the energy straggling. Bohr's theory is only valid for high energies in Beth-Bloch region where ion is stripped of all its electrons. Consequently, it fails to explain the lower energy case where the ion is not stripped off all its electrons. Corrections were then introduced by Lindhard and Scharff by extending Bohr's theory. For ion velocities below E_o [keV] = 75·Z_2 [Lin53], they obtained [Chu78]:

$$\Omega = \Omega_B^2 \frac{1}{2} L(\chi) \, for \, \chi \leq 3 \qquad (3.12)$$

$$\Omega = \Omega_B^2 \, for \, \chi \geq 3 \qquad (3.13)$$

where χ is a reduced energy variable given by:

$$\chi = v^2/Z_2 v_0 \qquad (3.14)$$

where v is the velocity of the projectile, $v_0 = e^2/h$ and $L(\chi)$ is the stopping number .

In our laboratory we employ the energy straggling values by Chu [Chu76]. Chu calculated energy straggling by using atomic charge distribution of the Hartree-Fock-Slater theory and incorporated them with Bonderup and Hvelplund's theory for energy straggling and also with the Lindhard and Winther stopping power theory [Bon71][Chu76][May77]. Chu's calculations gave straggling values which are much lower as compared with Bohr's calculations at low energies. The calculated straggling values can be found in a book written by Mayer *et al.* [May77].

3.6   Range and Range straggling

Energetic ions travelling inside a particular material travel in different directions and loose energy by electronic and nuclear stopping before coming to rest at a certain depth. The average distance travelled by the energetic ions from the surface to the point where they come to rest inside the material is called the range (R). It can be calculated using equation (3.15) which takes into account the stopping cross section. This can be written as [Lin63]:

$$R = \int_0^E \frac{dE}{-dE/dx} \tag{3.15}$$

The path of the energetic ions with high energy after penetrating the material is straight because electronic stopping dominates and no nuclear stopping is experienced. As the velocity decreases there are collisions with the target atoms and the ions experience a zigzag path when their energies are low. A diagram illustrating the path travelled by the ion is shown in figure 3-3. By taking into consideration all the above mentioned factors the total range of all the ions can be given as $R = R_{tot}/n = \Sigma l_i$, where n is the total number of ions implanted into the sample and l_i represents the different path lengths the ions travel inside the material.
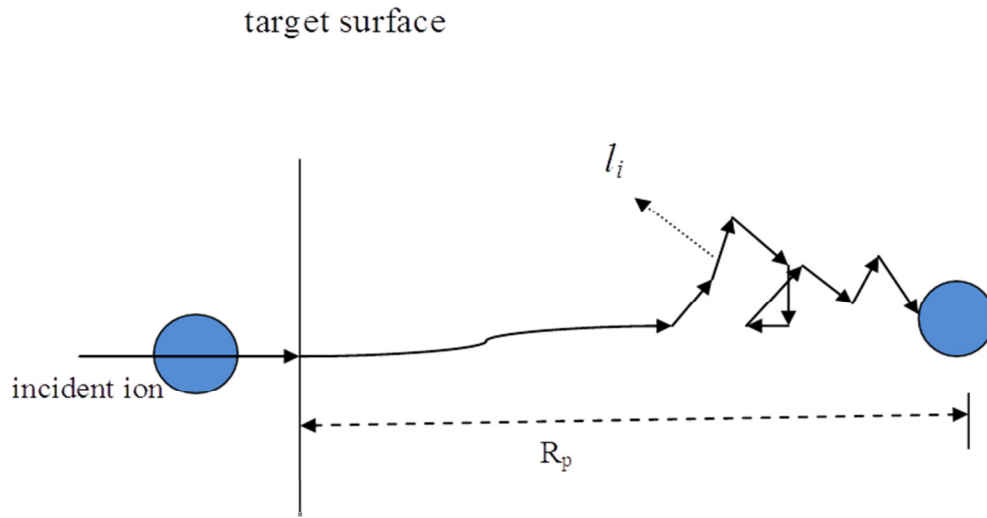
target surface

Figure 3-3: Schematic diagram for the path of the energetic ion inside the material.

The average range, measured parallel to the incident ion direction, of the ions penetrating the material from the target surface to where it comes to rest at a particular depth is called the projected range, R_P is shown in figure 3-3. The perpendicular range $R_\perp$ is measured perpendicular to the incident ion direction. The statistical deviation in the projected range distribution of the implanted ions with a given energy in a medium, due to statistical fluctuation in energy loss, is called the range straggling ΔRp. This range straggling ΔRp is fundamentally due to the multiple collisions of the ions which will result in the deviation of the ions from their original directions and lead to a spread in the range of the ion beam in the target [Tow94]. The ion concentration *N(x)* distribution of the implanted ion as a function of depth *x*, is often approximated to be Gaussian, written as [www2]:

$$N(x) = \frac{\Phi}{\sqrt{2\pi\Delta R_P^2}} \exp\{ -(x - R_p)^2 / 2\Delta R_p^2 \} \qquad (3.16)$$

where $N(x)$ is the ion concentration at depth x, Φ is the implanted fluence, R_P is the projected range and ΔR_p is the range straggling. A schematic diagram of the ion depth distribution is shown below. The FWHM can be calculated from the range straggling as shown in equation (3.11), in this case FWHM is directly proportional to the range straggling (ΔR_p).
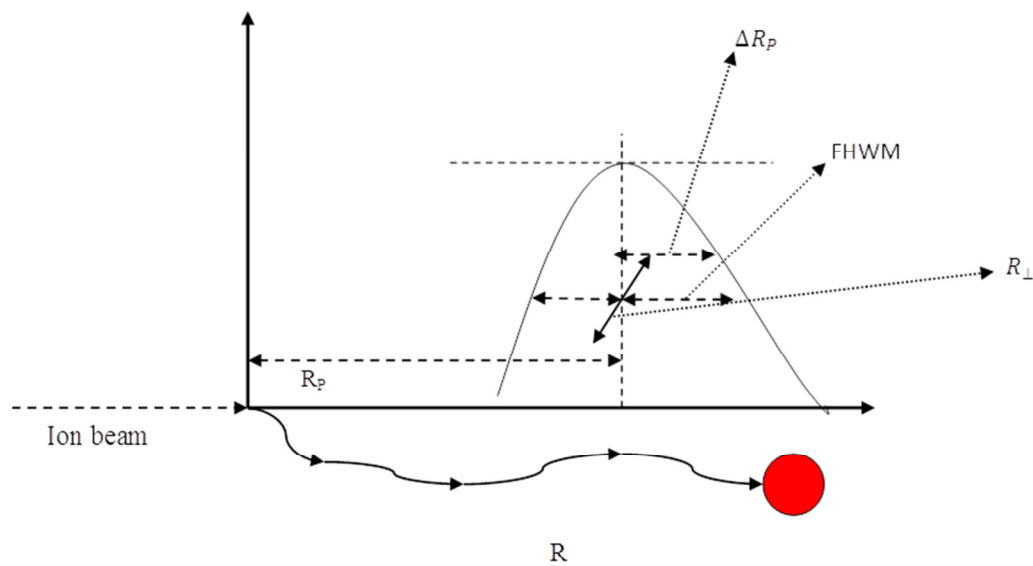

Figure 3-4: The schematic representation of the ion depth distribution and a path of an ion [Kui10].

3.7 SRIM

SRIM is a software concerning the Stopping and Range of Ions in Matter [Zei08] and it calculates the interactions of ions with matter. This program is based on a Monte Carlo simulation method, which uses binary collision approximation of with random selection of the impact parameter of the next colliding event [www3]. SRIM has an average accuracy of about 10% [Zie08]. When running the program certain parameters must be selected, i.e. the type of the ion you are using, the substrate and

energy of the ions. However, it doesn't take account of the crystal structure nor dynamic composition changes in the material that severely limits its usefulness in some cases [www4]. Other approximations of the program include [www4]:

- Binary collision i.e. only collisions between an ion and one substrate atom are considered.

- Recombination of knocked off atoms (interstitials) with the vacancies is neglected;

- the target atom which reaches the surface can leave the surface (be sputtered) if it has enough momentum and energy to pass the surface barrier.

- The system is layered, i.e. simulation of materials with composition differences in 2D or 3D is not possible.

- The threshold displacement energy is a step function for each element.

-

Several stopping theories are used in order to evaluate accuracy of the stopping power. The stopping power for all the ions are calculated in individual targets. The Brandt-Kitagawa theory and LSS theory are also used in calculations [Zie08]. SRIM applies the Core and Bond (CAB) approach for the calculation of ions in compounds, which is discussed in the paper by Ziegler *et al.* [Zie08]. The use of CAB approach produces corrections to the Bragg's rule and compounds having the common elements in compounds: H, C, N, O, F, S and Cl [Zie08].

3.8   References

[Bár86] G. Bárdos and G. M. Gavrilenko, Acta .Phys. Hung. 59 (1986)393.

[Blo33] F. Bloch, Ann. Phys.(Leipzig). 16 (1933) 285

[Bon71] E. Bonderup and P. Hvelplund, Phys. Rev. A4 (1971) 562.

[Chu76] W.K. Chu, Phys. Rev. **A13** (1976) 2057.

[Chu78] W. K. Chu, J. W. Mayer and M. A. Nicolet, "Backscattering Spectrometry", Academic Press, New York (1978) p.23 & 59

[Hla10] T. T. Hlatshwayo," Diffusion of silver in 6H-SiC", PhD Thesis, Department of Physics, University of Pretoria, (2010).

[Kui10] P.K. Kuiri, " Energetic Au irradiation effects on nanocrystalline ZnS films deposited on Si and Au nanoparticles embedded in silica glass" PhD Thesis, Institute of Physics Bhubaneswar, India, (2010).

[Lin53] J. Lindhard and M. Scharff, Met. Fys. Medd. Dan. Vid. Selsk. **27**, No. 15 (1953). p.28

[Lin61] J. Linhard, M. Scharff, Phys. Rev. 124 (1961) 128.

[Lin63] J. Linhard, M. Scharff and H.E. Schiott, Mat. Fys. Medd. Dan. Vid. Selsk 33, No.14 (1963).

[May77] J.W. Mayer and E. Rimini, "Ion beam handbook for material analysis", Academic Press, New York, (1977).

[Pet03] J. Peltola, "Stopping power for ion and clusters in crystalline solids", Accelerator Laboratory, University of Helsinki, Finland, (2003).

 [Tes95] J. Tesmer and M. Nastasi, " Handbook of Modern ion beam materials analysis", Materials Research Society, Pittsburg, (1995).

[Tow94] P. D. Townsend, P. J. Chandler and L. Zhang, "Optical effects of ion implantation", Cambridge University Press, New York, (1994). p32

[www1]

http://www.southalabama.edu/engineering/ece/faculty/akhan/Courses/EE539-   Fall04/Lecture-slides/Lecture-19-%20IMPLANTATION%20.pdf, 15July 2012.

[www2] http://personal.cityu.edu.hk/~appkchu/AP4120/9.PDF, 15 July 2012

[www3] http://en.wikipedia.org/wiki/Stopping_and_Range_of_Ions_in_Matter,04 December 2013

[www4] http://www.srim.org, 04 December 2013

[Zie85] J. F. Ziegler, J. P. Biersack, U. Littmark, "The stopping and range of ions in matter", Pergamon Press, New York (1985).

[Zie08] J. F. Ziegler, J. P. Biersack, M.D. Zeigler, "The stopping and Range of Ions in Matter", Ion Implantation Press, U.S.A (2008).

[Zol05] Z. Zolnai, "Irradiation-induced crystal defects in silicon carbide" PhD Thesis, Department of Atomic Physics, Budapest University of Technology and Economics, (2005).

CHAPTER 4

RUTHERFORD BACKSCATTERING SPECTROMETRY (RBS)

Rutherford Backscattering Spectrometry (RBS) is an ion scattering technique for quantitative composition analysis of thin layers or near surface regions of solids. It allows fast non-destructive analysis of materials and multi-element depth concentration profiles. This technique is based on the analyses of the energy of backscattering particles. The typical particles that are normally used in RBS are helium (He) and hydrogen (H) ions. In our experiments we used alpha particles, i.e. He$^+$. Consequently, in our discussion we shall use alpha particles as the bombarding beam. When incoming energetic He$^+$ particles strikes the target material, the alpha particles will lose energy as they penetrate the target and come to rest inside the material. A minority of the particles are backscattered. Some of the backscattered particles can be detected by the detector depending on their backscattering angle. The detector is normally placed at an angle greater than 90° and less than 180° to the incoming beam (as shown in figure 4.1). From these detected backscattered particles different information of the target can be deduced: mass and depth distributions of the target elements. In this chapter the important RBS parameters are firstly discussed followed by those for RBS-C (RBS in a channeling mode).

4.1 Kinematic Factor

The kinematic factor is defined as the ratio of the backscattered alpha particle's energy E_1 after collision to the incident energy E_o before the collision. It is given by [Chu78][Gro84][May77][Tes95]:

$$K = \frac{E_1}{E_0} = \left[\frac{M_1 \cos\theta \pm \sqrt{M_2^2 - M_1^2 \sin^2\theta}}{M_1 + M_2} \right]^2 \qquad (4.1)$$

where M_1 and M_2 are atomic masses of the alpha particle and target atom respectively, E_o and E_1 are the energies of the incident and backscattered alpha particle respectively and θ is the backscattered angle (as shown in figure 4.1).

The plus sign in equation (4.1) is used when $M_1 < M_2$, while the minus sign is used when $M_1 > M_2$. In our case the plus sign is applicable because the mass of the target atom is greater than that of the alpha particles. The angle, θ, is fixed.
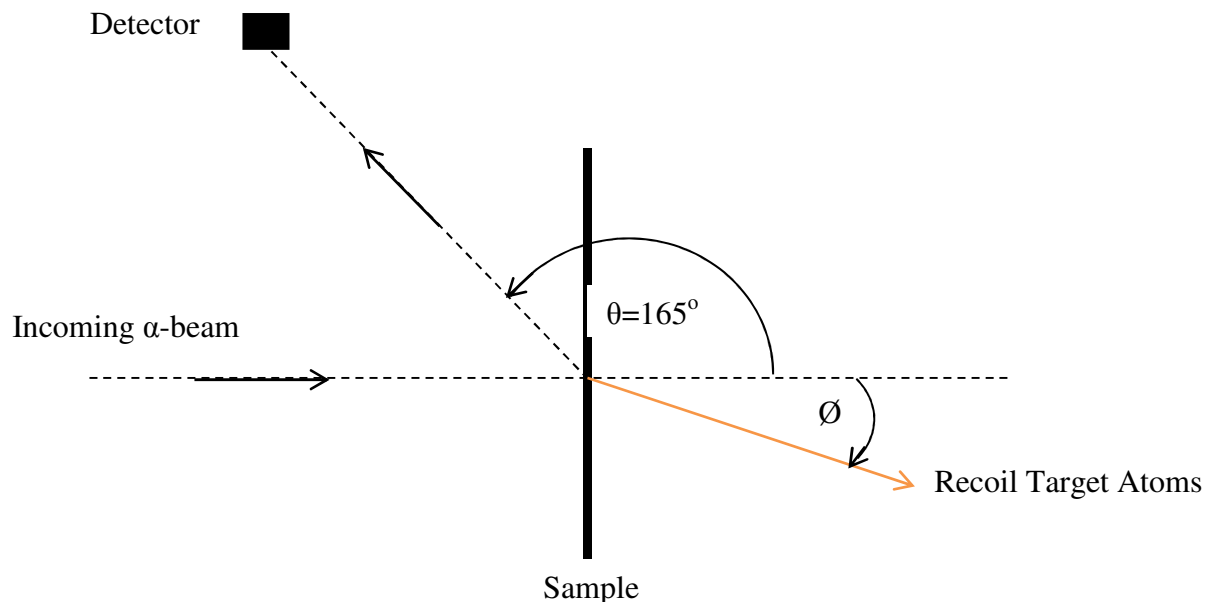

Figure 4-1: *A schematic diagram showing the RBS experimental setup at the University of Pretoria and the backscattering angle θ [Hla10]*

4.2 Differential Cross Section

The differential cross section for scattering i.e. $d\sigma/d\Omega$ in a given direction into the detecting solid angle $d\Omega$, is defined as the number of particles scattered into a solid angle $d\Omega$ per number of incident particles per unit area. The differential cross section for the scattering angle of a projectile into a solid angle $d\Omega$ centered around an angle θ in the laboratory coordinate system is given as [Chu78][Tes95]:

$$\left(\frac{d\sigma}{d\Omega}\right)_{projectile} = \left(\frac{Z_1 Z_2 e^2}{4E_o}\right)^2 \frac{4\left(M_2 cos\theta + \sqrt{M_2^2 - M_1^2 sin^2\theta}\right)^2}{M_2 sin^4\theta \sqrt{M_2^2 - M_1^2 sin^2\theta}} \tag{4.2}$$

where Z_1 is the atomic number of the projectile with mass M_1, Z_2 is the atomic number of the target with mass M_2, E_o is the energy of the projectile before scattering, e is the electron charge and θ is the back scattering angle.

The differential cross section has a proportionality relation with the atomic number of the target Z_2 i.e. ($d\sigma/d\Omega \propto Z_2^2$), which means the RBS is more sensitive to heavy elements as compared to light elements. The inverse proportionality of E_o to the differential cross section i.e. ($d\sigma/d\Omega \propto \frac{1}{E_o}$), shows that as the energy increases the backscattering yield decreases.

The total number of backscattered and detected particles is given by:

$$A = \sigma \Omega Q N \tag{4.3}$$

where Ω is the detector solid angle, N the total number of atoms per unit area, Q is the total number for incident projectiles, σ is the differential cross section averaged over the surface of the detector. From equation (4.3) we can see that if $A, \sigma, \Omega \ and \ Q$ are known we can obtain N.

4.3 Depth Profiling

The backscattered alpha particles from different depths within the target material have different energies. The incident particle of energy E_o that backscatters at the surface has energy of KE_o, where K is the kinematic factor discussed in section 4.1. This incident particle energy E_o loses some of its energy as it penetrates (inward). It has energy E immediately it undergoes backscattering at depth x (shown in figure 4-2)[Chu78]. Thus E_o is greater than E. The particle backscattered at depth x also loses

energy as it goes out. The particle emerging from the surface has energy E_1. Therefore, E_1 is less than E.
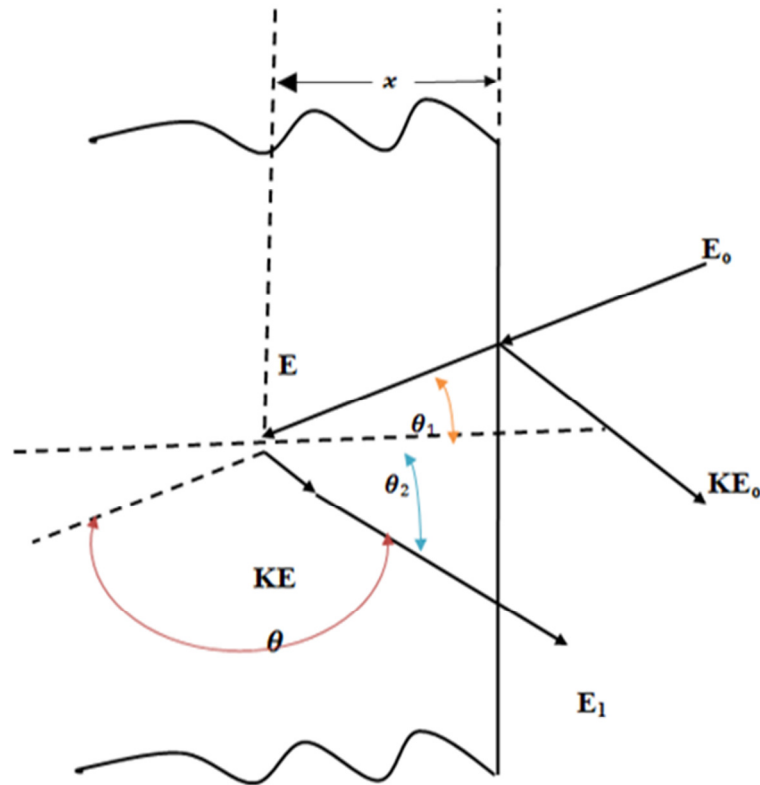

Figure 4-2: A schematic diagram illustrating the backscattering event of alpha particles and energy loss from depth x [Chu78]

From figure 4-2 the energy E with the inward path when the alpha particle losses energy can be related to $x/cos\theta_1$ by [Chu78]:

$$x/cos\theta_1 = -\int_{E_o}^{E} dE/(dE/dx) \tag{4.4}$$

Similarly, the outward path is related to KE and E_1 by:

$$x/cos\theta_2 = -\int_{KE}^{E_1} dE/(dE/dx) \tag{4.5}$$

The energy difference E_o-E is the energy loss along the inward path ΔE_{in}, and KE-E_1 is the energy loss along the outward path ΔE_{out}. The alpha particles backscattered at the surface have the energy of KE_o. Making an assumption that dE/dx has a constant

value along the inward and outward paths, equations (4.4) and (4.5) reduce to [Chu78]:

$$E = E_o - \frac{x}{\cos\theta_1} \left.\frac{dE}{dx}\right|_{in} \tag{4.6}$$

and

$$E_1 = KE - \frac{x}{\cos\theta_2} \left.\frac{dE}{dx}\right|_{out} \tag{4.7}$$

Here the subscripts 'in' and 'out' refer to the constant values of *dE/dx* along the inward and outward paths. By elimination of *E* from equation (4.6) and (4.7) we have:

$$KE_o - E_1 = \left[\frac{K}{\cos\theta_1} \left.\frac{dE}{dx}\right|_{in} + \frac{1}{\cos\theta_2} \left.\frac{dE}{dx}\right|_{out} \right] x \tag{4.8}$$

where KE_o is the energy of the backscattered alpha particles at the surface atoms of the target and E_1 is the energy of the backscattered alpha particle from the atom at depth *x*.

Taking ΔE to be the energy difference between E_1 and KE_o i.e.

$$\Delta E = KE_o - E_1 \tag{4.9}$$

Then equation (4.8) can be written as:

$$\Delta E = [S]x \tag{4.10}$$

where

$$[S] = \left[\frac{K}{\cos\theta_1} \left.\frac{dE}{dx}\right|_{in} + \frac{1}{\cos\theta_2} \left.\frac{dE}{dx}\right|_{out} \right] \tag{4.11}$$

[S] is called the energy loss factor which contains the relationship between the energy and the depth information. Thus a measured energy spectrum can therefore be directly converted into a depth scale.

4.4 Channeling

When an energetic ion beam is directed along a major crystalline direction of a single crystal, the Channeling process occurs. During this process, ions are steered into open spaces between close-packed planes of atoms in a crystal by means of a correlated series of small-angle collisions. This results in a reduction of backscattering yield. Consequently Channeling is very sensitive to crystal defects.

The open channels in a crystal are categorized into two groups, viz. axial and planar channels. The axial channel is defined by rows of atoms around the trajectory, and the planar channel is defined by parallel planes of atoms. Figure 4-4 shows the channeling spectra of axial and planar alignment, where χ_{MIN} is the minimum yield, which is the ratio between the aligned and random yield near the surface. The axial alignment in the spectrum has damped yield oscillation near the surface region and has a lower minimum backscattering yield. Planar alignment has clear yield oscillations near the surface region and has high backscattering yield [Bir89].
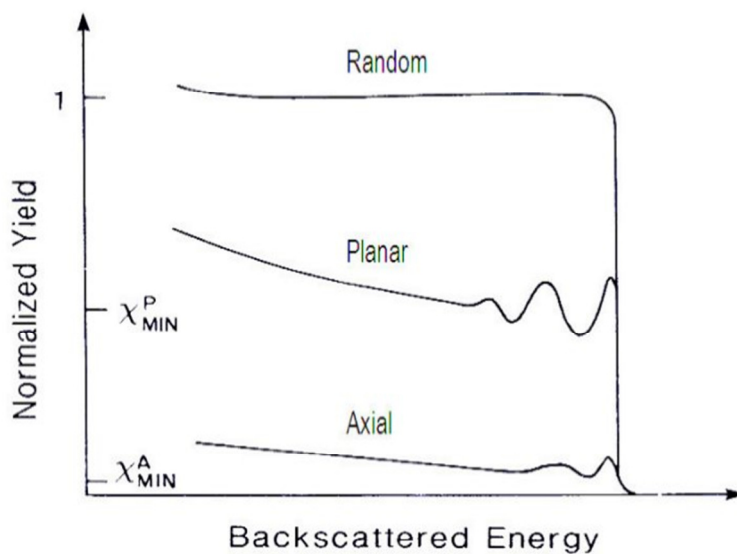

Figure 4-3: *RBS channeling spectra showing of axial and planar channeling. χ_{MIN}^{P} and χ_{MIN}^{A} are the planar and axial minimum yield[Bir89].*

For channeling to take place, the ion incident angle upon a channel of atoms must be smaller than the critical angle ψ_{c} [Lin65]. The critical angle is given by:

$$\psi_c = \left(\frac{2Z_1 Z_2 e^2}{E_0 d}\right)^{\frac{1}{2}} \tag{4.12}$$

where E_o is the incident energy of the ion, d is the atomic spacing along the aligned row and Z_1 and Z_2 is the atomic number of the ion and target respectively. ψ_c is a theoretical parameter and is directly proportional to the angular half width at half $\psi_{1/2}$ of the angular scan profile (see figure 4.4). χ_{MIN} in figure 4-4 is the minimum yield. Dechanneling occurs when some of the channeled ions are scattered away as they penetrate into the solid during the channeling process. It is due to the presents of defects such as substitution impurities, interstitial atoms and displaced lattice atoms (figure 4-5). In this case there will be an increase in the backscattering yield.

Figure 4-4: *The angular yield about an axial channel (solid curve) and a planar channel (broken line) [Bir89].*
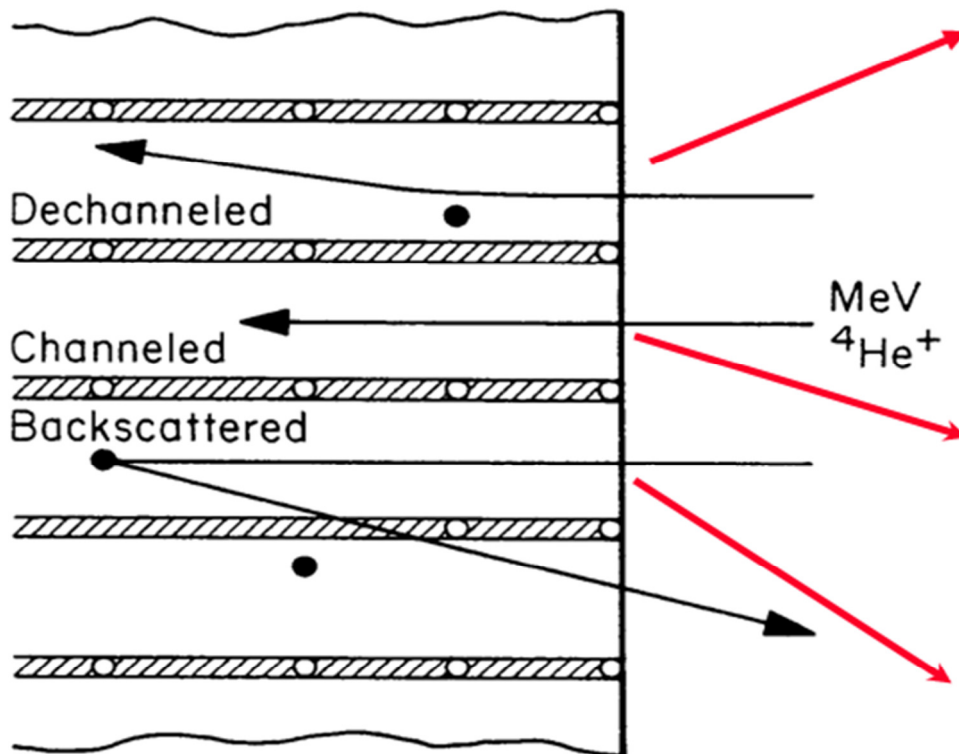
Dechanneling by defects

Figure 4-5: Schematic representation showing channeling, dechanneling and direct backscattering by interstitial atoms [www1].

Lindhard's work [Lin64] introduced the continuum model which describes channeling in a continuum description of atomic strings (axial channeling) and planes (planar channeling). This model forms the basis for current investigations and analyses of channeling. The continuum model is based on continuum potentials obtained by averaging the lattice potentials over atomic strings or planes. Thus, this model of channeling assumes that ion-string or ion-plane scattering (illustrated in figure 4-6) can be approximated by scattering from a string or plane of uniform potential, thereby assuming that the discrete nature of atoms is insignificant. This continuum potential is given as [Gro84][Bir89][Tes95]:

$$U(r) = \frac{1}{d} \int_{-\infty}^{\infty} V\left[(z^2 + r^2)^{\frac{1}{2}}\right] dz \tag{4.13}$$

Where *V* is the interatomic potential and *d* is the distance between the particles, *r* is the height and *z* is the direction in which the particles move, as shown in figure 4-6 below.
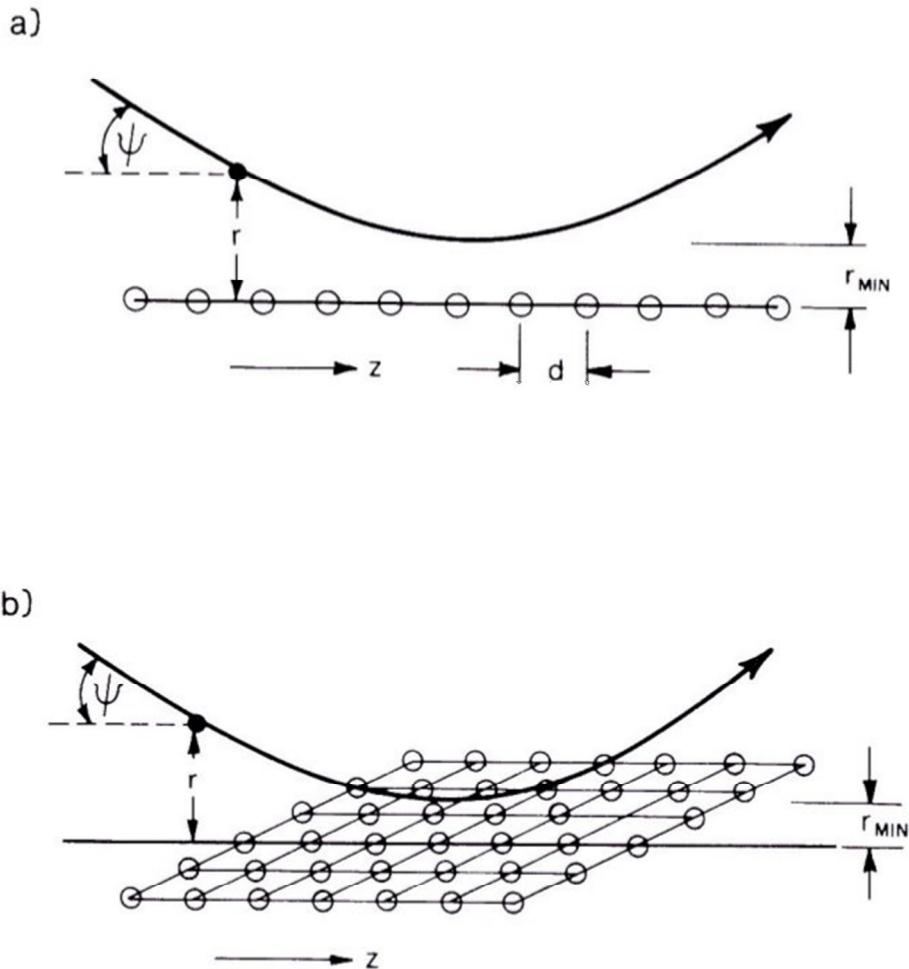

Figure 4-6: *Continuum model of channeling (a) Ion scattering from an axial string of atoms (b) Ion scattering from a plane of atoms [Bir89].*

When ions are implanted in a material, damage is created (i.e. the implanted ions displace the host/target material atoms from their original lattice site distorting the structure and creating vacancies and interstitials. Rutherford backscattering in a channeling mode (RBS-C) helps us to study this damage. This channeling technique gives information of the amount and depth distribution of the damage created in the material. The radiation damage created during implantation differs according to the fluence and temperature of implantation. The random and aligned spectrum gives us information, on whether the material is amorphous (and if so shows the thickness of the amorphous layer) or whether the material retained its crystallinity with some

41

damage created. In this thesis RBS-C is used to study the radiation damage retained after implantation of xenon into 6H-SiC at 600 ^{o}C and after annealing.

4.5 Van de Graaff

The basis of the RBS technique hinges on the analysis of the energy from the backscattered charged particles in any given material. The energetic particles are generated by particle accelerators such as a Van de Graaf accelerator (used in this project). The Van de Graaff is a high-voltage electrostatic generator that serves as a type of particle accelerator. It is made of two electrodes, a belt (made of silk or other high dielectric material), and metal pulleys surrounded by hollow metal sphere and ion source. A diagram representing the typical Van der Graaff accelerator is shown below.
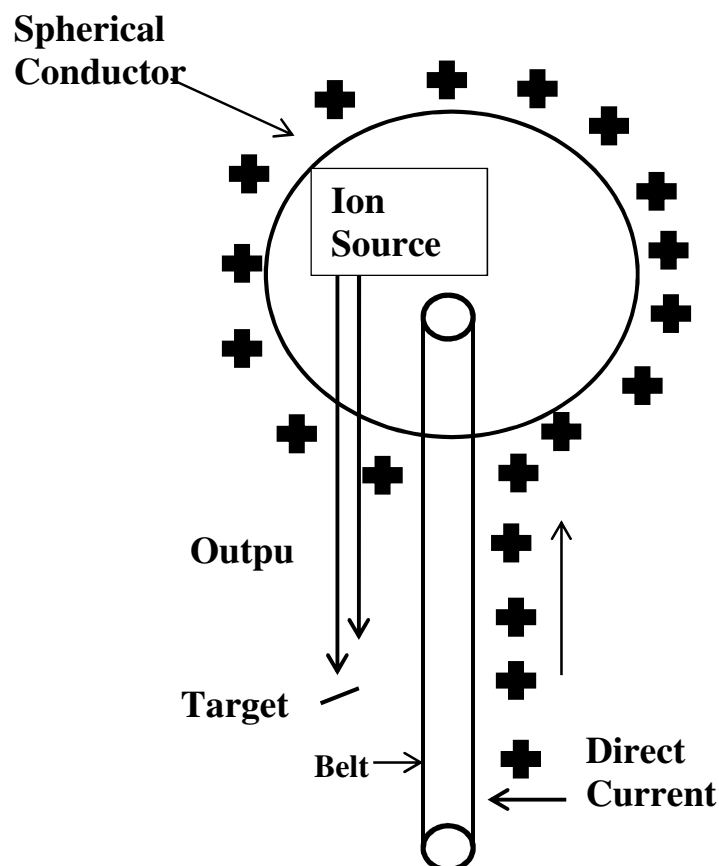

Figure 4-7: Schematic diagram of a Van de Graaff accelerator [www2].

In figure 4-7 the two electrodes are located at the base inside the metal sphere attached to one end of an insulating column. The ion source, (rf ion source shown in figure 4-8) located inside the high-voltage terminal, generates the charged particles. The electric voltage between the high-voltage supply and ground allows the charged particles to be accelerated from the ion source. The Corona needles remove the charge from the belt, and uniformly distribute it over the surface of the metal sphere.

The experiments in this dissertation were performed using the Van de Graaff accelerator at University of Pretoria. The maximum voltage of this machine is 2.5 MeV but for this investigation energy of 1.6 MeV was used. The ions accelerated were He^+. Beam currents up to 100 µA can be obtained. A schematic diagram of the accelerator is shown in figure 4-9 and the rf ion source 4-8 below.
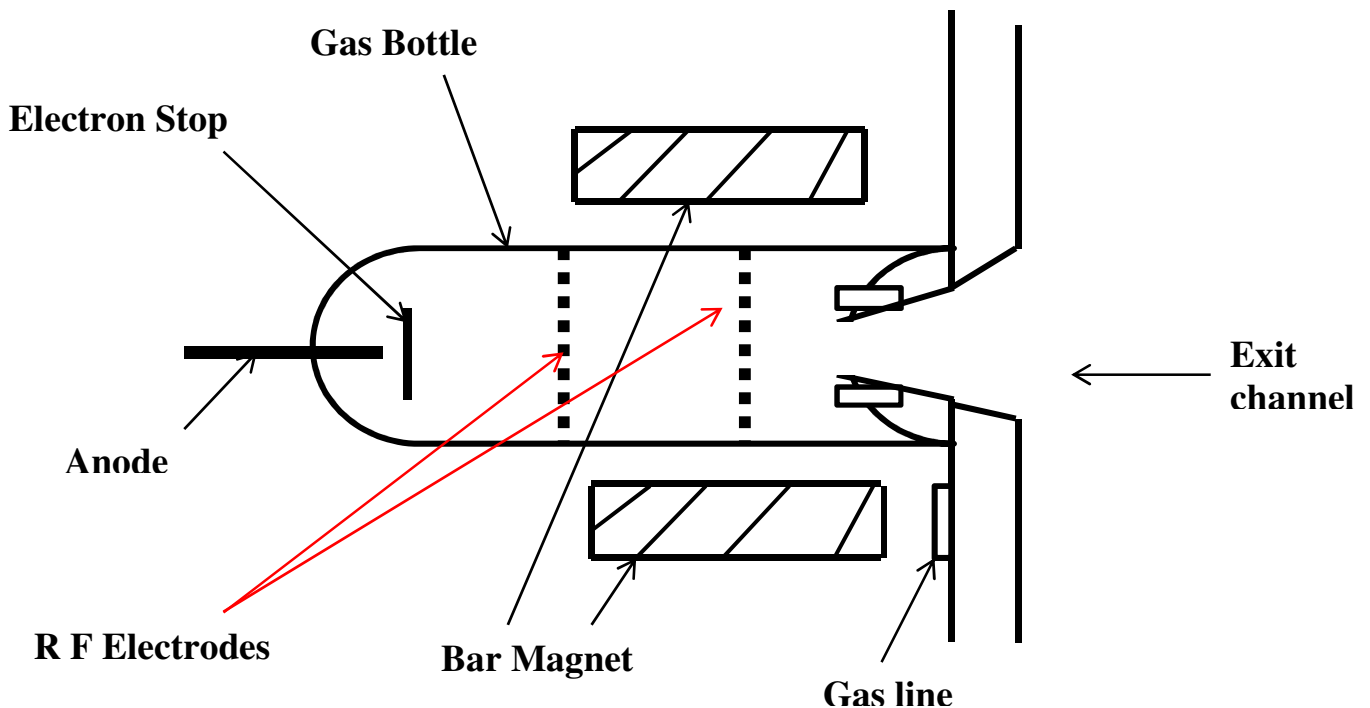

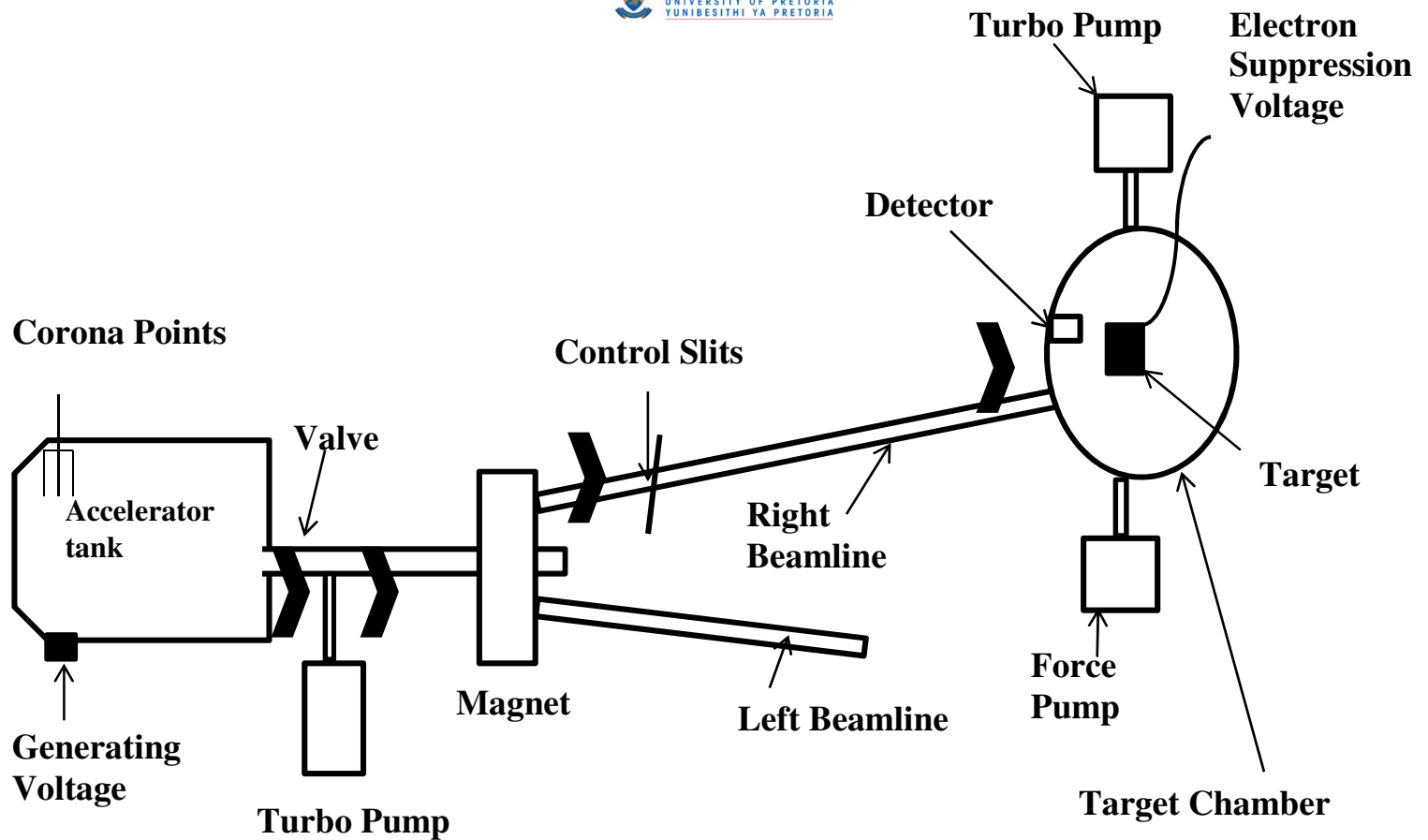*Figure 4-8*: *Schematic diagram of the rf ion source [Chu78].*

Figure 4-9: Schematic diagram of the van de Graaff accelerator of the University of Pretoria [Kuh10].

To produce a monochromatic beam consisting only of one specific ion (He^+) a dipole deflection magnet is applied as mass and charge state separator. It deflects the beam into either left beam line or right beam line. For our experiments the right beam line was used. The combination of vertical and horizontal slits guides the beam to the sample chamber allowing for collimation and focusing. The sample is fixed on a stainless steel sample holder connected to the three axis goniometer system. The backscattering alpha particles are detected by a Si-surface barrier detector. The output charge signal is transferred to the pre-amplifier, and is integrated into a voltage signal. The voltage signal is then amplified by the amplifier then digitized by an analogue to digital converter inside the multi-chamber analyzer (MCA) and stored in a computer which is connected to the MCA. A spectrum of counts vs. channel is obtained. The data acquisition is discussed in section 5.4.

44

4.6 References

[Bir89]   J. R. Bird and J. S. Williams, "Ion Beam for Material Analysis", Academic Press, Australia (1989) p.620

[Chu78] W. K. Chu, J. W. Mayer and M. A. Nicolet, "Backscattering Spectrometry", Academic Press, New York (1978) p.23 & 59

[Gro84] J. J. Grob and P. Siffert, Cryst. Growth. 8 (1984) 59.

[Hla10] T. T. Hlatshwayo," Diffusion of silver in 6H-SiC", PhD Thesis, University of Pretoria, Department of Physics, (2010).

[Kuh10] R. J. Kuhudzai, " Diffusion of ion implanted iodine in 6H-SiC" Msc dissertation, University of Pretoria, Department of Physics, (2010)

[Lin64] J. Lindhard and A. Winther, Mat. Fys. Medd. 34 (1965) No.4

 [Lin65] J. Lindhard, K. Dan. Vidensk. Selsk, Mat. Fys. Medd. 34 (1965) No.14, p.11 and 13

[May77] J.W. Mayer and E. Rimini, "Ion Beam Handbook for Material Analysis", Academic Press, London (1977) p.43

[Tes95] J. R. Tesmer and M. Nastasi,"Handbook of Modern Ion Beam Materials Analysis", Materials Research Society, Pittsburgh (1995) p.40

[www1] https://sites.google.com/a/lbl.gov/rbs-lab/ion-beam-analysis/ion-channaling, 11 September 2012

[www2] http://www.lbl.gov/abc/wallchart/chapters/11/2.html , 11 September 2012

CHAPTER 5

EXPERIMENTAL PROCEDURE

5.1   Sample preparation

The starting material in this study was a single crystalline 6H-SiC wafer produced by Cree Inc[®]. The thickness of the wafer was 0.3 mm with a diameter of 50 mm. Before implantation, which is discussed in section 5.2, the 6H-SiC wafer was cut into two and cleaned by a sequence of ultrasonic agitation in acetone, followed by deionised water and methanol to remove the grease and physical contamination from the surface of the wafer.

After implanting xenon into the SiC wafer, the SiC wafer was cut to a size suitable for the sample holder for the RBS-C analysis. Crystalbond 509[TM] glue was used to glue the wafer to the brass disc. The glue was placed on the brass disc, which was then heated until it melted. After it had melted, it was then spread over the brass disc and the wafer was placed on the brass disc. The glue was allowed to cool down so that the wafer was strongly attached to the brass disc. The brass disc was then placed in the cutting machine for the wafer to be cut into small equal pieces of approximately 5.5 mm × 5 mm, producing rectangular samples. Water was used as a lubricant for the diamond blade to wash away debris. It was cut slowly to reduce damage created to the wafer.

The samples were then cleaned using an ultrasonic bath with acetone for 3 to 4 min four times to remove the glue. Then it was washed with MA 02 soap, after which it was repeatedly rinsed with deionised water. Methanol was used, also four times, to remove the excess water from the sample and then the methanol was blown away by nitrogen gas.
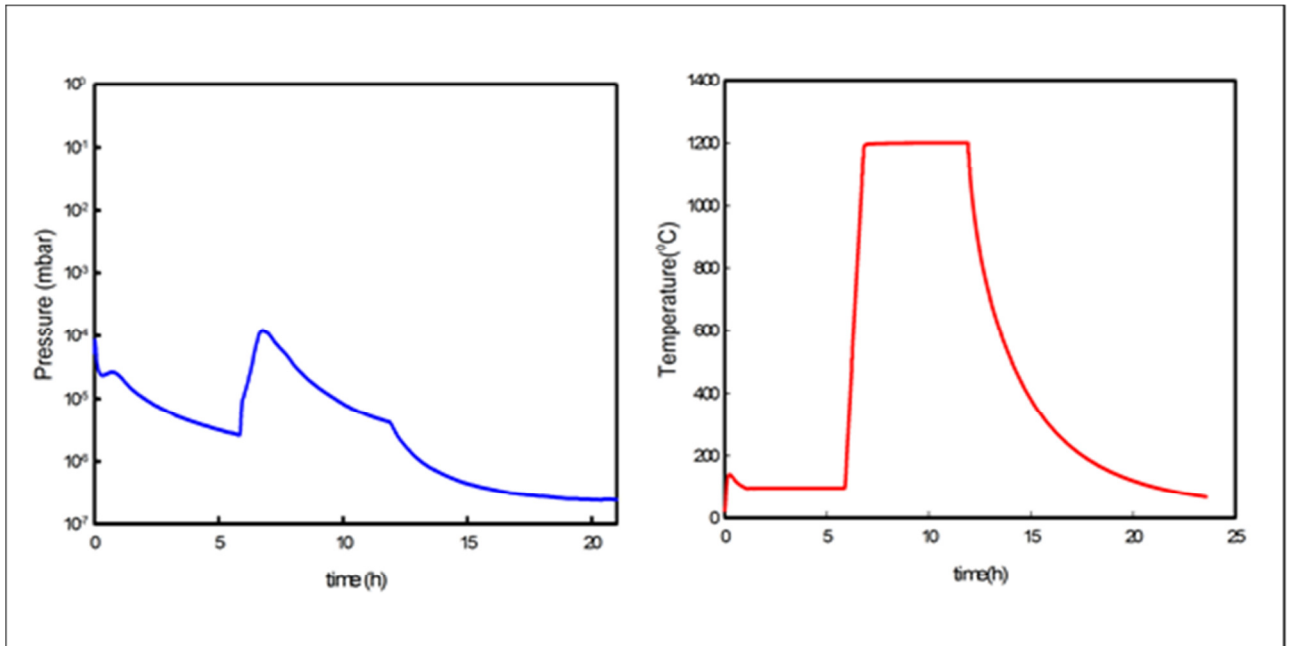
5.2 Xenon implantation

Implantation was performed in the Institute für Festkörperphysik, Friedrich-Schiller-Universität, Jena, Germany. The xenon ions (^{136}Xe) were implanted with a fluence of 1×10^{16} cm^{-2} at the energy of 360 keV into 6H-SiC at 600 ^{o}C. The flux was maintained at a rate below 10^{13} cm^{-2} s^{-1} to avoid beam induced target heating of the sample. The incident angle was set to be 7° with respect to the normal incident, so as to avoid channeling from taking place during implantation.
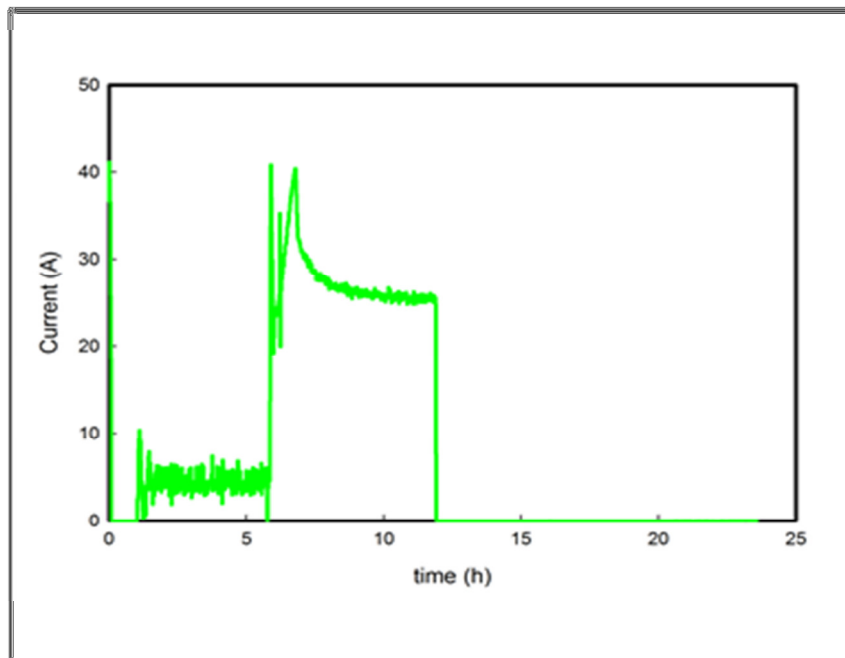
5.3 Annealing of the samples

Isochronal vacuum annealing from 1000 °C to 1500 °C in step of 100 °C for 5h with pressure of the order of 10^{-5} mbar are reported in this study. The annealing was performed using a computer controlled Webb77 graphite furnace with a maximum temperature of 2300 ^{o}C. Before putting the samples inside the oven, they were first placed inside a graphite crucible to avoid contamination of the samples with any contaminants in the oven. The temperature of this oven is controlled by a Eurotherm 2704 controller which is connected to a thermocouple and pyrometer. The temperature measured by the thermocouple is up to 1475 ^{o}C and for temperatures higher than 1525 ^{o}C, a pyrometer is used. An average value of the pyrometer and thermocouple values was used between these temperatures, i.e. for the 1500 ^{o}C annealing.

Figure 5-1, represents the pressure (a), temperature (b) and current(c) curves for the heating furnace as a function of time. Degassing was performed to limit the high pressure peaking during annealing and to cut down the pumping time. Degassing took place at 100 ^{o}C for about 6 hours, to facilitate the release of water vapour and other gasses present in the high temperature carbon insulator in the oven. The degassing phase was from 0 to about 6 hours as seen in the graph (b). During the pump down period, the pressure decreased exponentially for a constant pumping speed in accordance with normal vacuum theory [Har89]. In this region, the pressure was initially in the 10^{-4} mbar range. After the heating element was switched on, the pressure had a small peak.

47

(a)

(b)

(c)

Figure 5-1: Vacuum pressure (a), temperature (b) and current (c) curve as function of time for a 5h annealing at 120 0⁰C.

48

This small increase in pressure was due to the degassing of the heating filament and the parts of the vacuum system which were heated by the heater. Because the total degassing rate was higher than the pumping rate, it led to this small pressure peak.

After degassing a current of about 40A was measured as the temperature was increased to 1200 $^{\circ}$C, but then dropped to 28A to maintain the final temperature for 5h. Heating of filament and the vessel walls near the heating filament due to the large current caused the initial high degassing rate of the vacuum system which resulted in a steep increase in the vacuum pressure from 10^{-6} mbar to about 10^{-4} mbar. The pressure increased almost linearly as a function of time to a maximum value of about 10^{-4} mbar at the beginning of annealing. During the heating ramp the heating rate was 20 $^{\circ}$C/min. The temperature remained constant while a decrease in pressure (from 10^{-4} to 10^{-5} mbar) took place during the 5h annealing period while the current was stable at 28A.

The current was turned off when annealing time ended. The system was allowed to cool down to about 40 $^{\circ}$C. Argon gas was then let into the furnace to break the vacuum. After removing the sample, the chamber was flooded with argon gas to limit the absorption of water vapour as well as other atmospheric gases present.

5.4   Data Acquisition

A block diagram for RBS electronic circuit is shown in figure 5-2 below. The backscattered alpha particles are detected by a surface barrier detector located at an angle of 165° relative to the incident beam. The output charge signal of the detector is fed into the Canberra pre-amplifier where it is integrated into a voltage signal. Both the charge and voltage signals are proportional to the energy of the backscattered particles. The detector is supplied with a bias voltage of 40 V from a Canberra 30102D high voltage supply. The voltage signal from the pre-amplifier is then fed into the Tennelec TC 243 amplifier for further amplification. A bipolar output signal produced from the amplifier is then fed into the digital oscilloscope to monitor the shape of the output pulse, while the unipolar output signal is fed into the multichannel analyser (MCA).

At the same time, current is collected at the back of the target and transported to the Ortec 439 current integrator. From the current integrator a logical signal is delivered to the charge counter and from there it is delivered to the MCA and the counter. The logic signal from this current commands the counter when to start and stop counting. It also directs the MCA when to start and stop processing the unipolar signal from the amplifier. A single channel analyser (SCA) inside the MCA selects the desired energy range which can be processed by adjusting the lower and upper energy discriminators in the MCA. The output of the MCA is fed to the computer, where it is recorded as yield versus channel number spectrum.
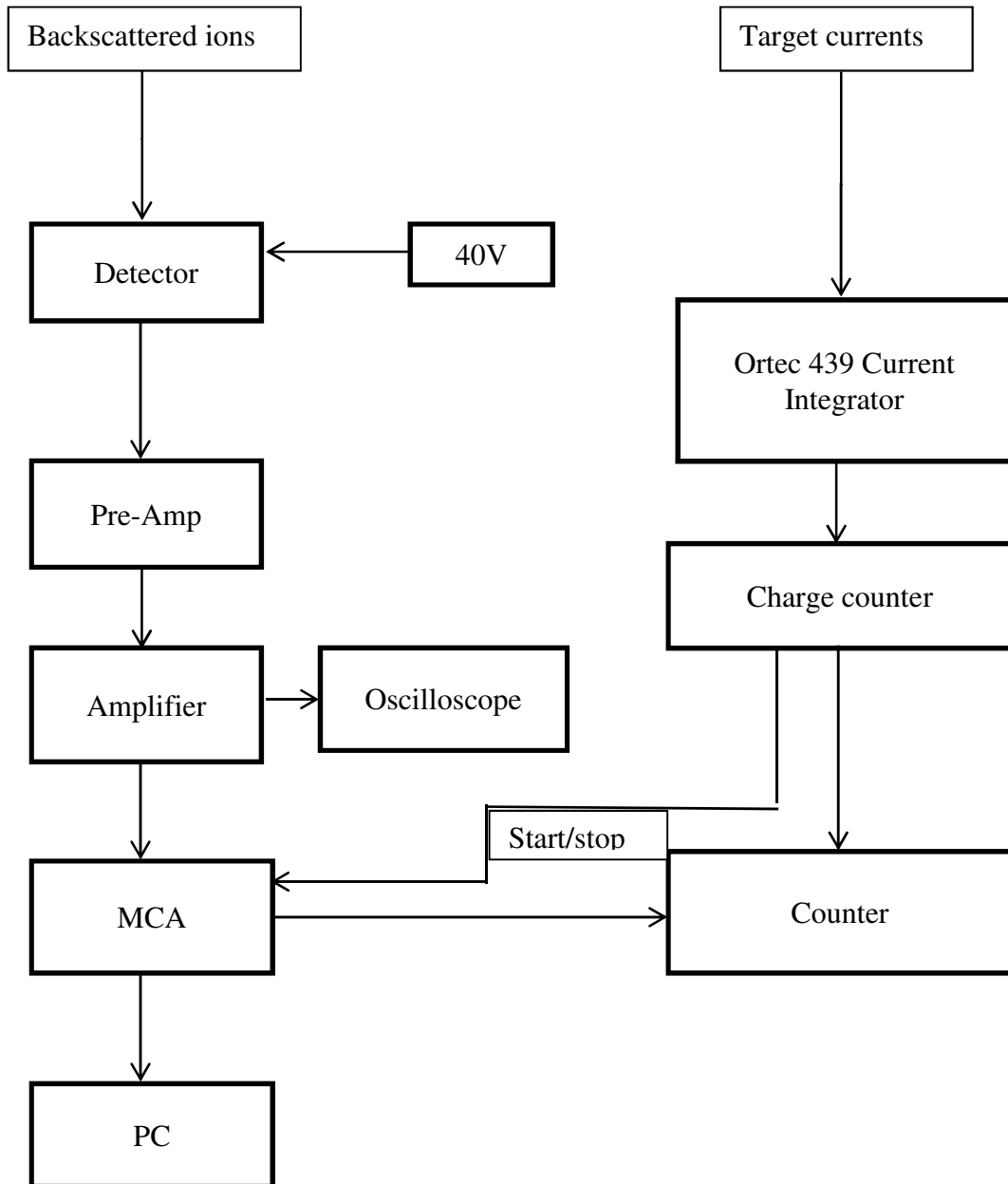
Figure 5-2: Block diagram for the RBS electronic circuit in University of Pretoria.

5.5 Data Analysis

A spectrum of counts versus channel number obtained by collecting a charge of $8\mu C$ constituted a run. Runs at two energies which are 1.4MeV and 1.6MeV from the RBS spectrum were used in order to be able to calculate the energy calibration required for depth profile analysis. The energy calibration is given in keV/channel. Using a computer program called STOP2 [Fri09] which makes use of energy loss data given in Ziegler [Zie77], the energy calibration was converted to into depth calibration which is given in nm/channel.

The spectra of the counts versus depth (nm) of the xenon peak were fitted to an Edgeworth distribution using the computer program GENPLOT [www1] to obtain these moments: projected range (R_p), range straggling/ standard deviation (ΔR_p) , skewness *(γ)* and kurtosis *(β)*. The projected range is the average range, measured parallel to the incident ion direction, of the ions penetrating the material from the target surface to where it comes to rest at a particular depth. The full width at half maximum *(FWHM)* of a Gaussian distribution is calculated using the standard deviation, σ, and written as:

$$FWHM = 2R_P \sqrt{2ln2}.$$

(5.1)

Kurtosis measures whether the data obtain are peaked or flat relative to a Gaussian distribution. When the value is three it means the peak is a Gaussian distribution. Skewness measures how asymmetric a distribution can be. The skewness can either indicate a positive or negative skewness distribution. A positive skewness tells us that the asymmetric distribution tails towards the more positive values, while on the negative skewness it tails towards the more negative values compared to the projected range position.

5.6   References

[Fri09]   E. Friedland, STOP2, Private Communication, Department of Physics, University of Pretoria, (2009).

[Har89]   NS Harris, "Modern Vacuum Practice", McGraw-Hill, London, 1989

[www1]   www.genplot.com, 6 June 2012.

[Zie77]   J. F. Ziegler, "The Stopping and Ranges of Ions in Matter", Pergamon Press, New York (1977).

CHAPTER 6

RESULTS AND DISCUSSION

The diffusion of xenon implanted into 6H-SiC at 600 ^{o}C was investigated using Rutherford backscattering spectroscopy (RBS). Rutherford backscattering spectroscopy in a channeling mode (RBS-C) was used to investigate the effect of radiation damage. An RBS spectrum of SiC implanted with Xe at 600 °C is shown in figure 6.1. The analysis was done at the energy of 1.6 MeV using He^{+} particles and at a scattering angle of 165°. The surface positions of the elements are indicated by the arrows. The surface position in the RBS spectrum of each element is given by the product of kinematic factor, K (of the element) and the α-particle incident energy, E_o as explained in chapter 4. The kinematic factor is influenced by the weight i.e. mass of the element M_2 of the target atoms as can be seen from the ideal backscattering case where θ = 180º and the kinematic factor equation given in (4.1). In RBS spectrum the channel number is equivalent to the backscattered energy i.e. KE_o. Hence Xenon appears at the highest channel number.

In the RBS spectrum- see figure 6.1, the carbon RBS profile is superimposed by the Si profile, because some of the backscattering ions from Si atoms deep inside the SiC that have the same energy as those backscattered from more shallow carbon atoms.

In this dissertation, the diffusion of xenon implanted into 6H-SiC at 600 ^{o}C with a fluence of 1 × 10^{16} cm $^{-2}$ and the effect of radiation damage on the diffusion were investigated using RBS and RBS-C. This was achieved by vacuum annealing the samples at temperature ranging from 1000 ^{o}C to 1500 ^{o}C for 5 h in steps of 100 °C.
In this chapter results are presented and discussed in the following format: In section 6.1 radiation damage results are discussed and in 6.2 diffusion results are discussed.
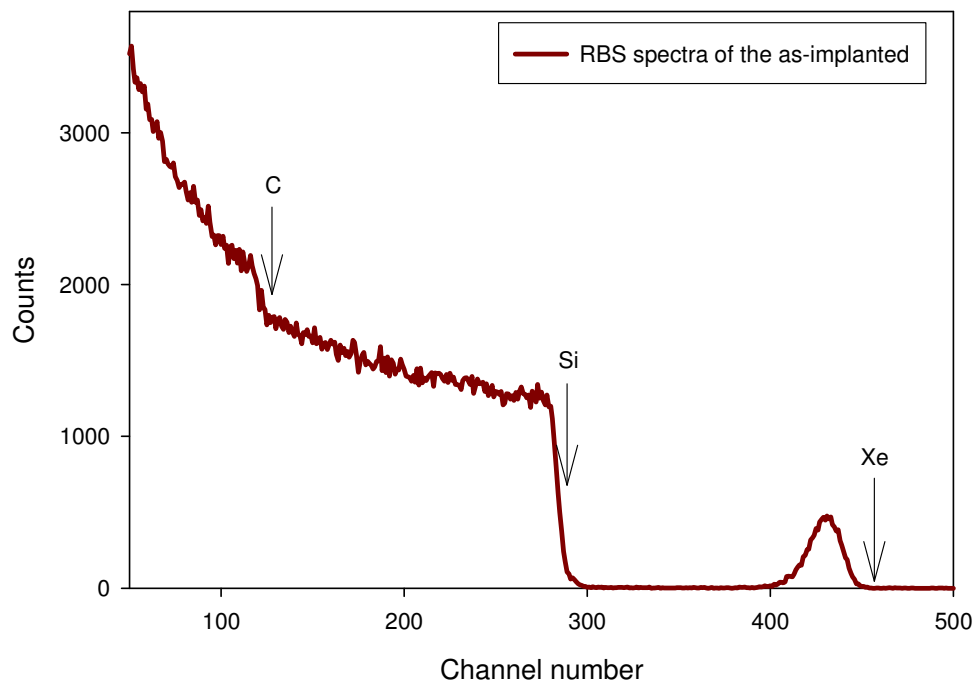
Figure 6-1: Aligned RBS spectra of Xe implanted in 6H-SiC at 600 ^{o}C. The arrows show the surface position of each of the elements.

6.1 Radiation Damage Results

The aligned spectra of Xe implanted at 23 ^{o}C, 600 ^{o}C and unimplanted samples compared to the random spectrum are depicted in figure 6-2. The main focus is on the 600° C implantation, while the room temperature (23 ^{o}C) implantation is only included for comparison.

The aligned spectrum of the sample implanted at 23 ^{o}C overlaps the random spectrum indicating that an amorphous region from the surface up to approximately 200 nm was formed during implantation. When comparing this depth with the typical projected range R_p = 112.4 nm and the range straggling of ΔR_p =28.7 nm, it follows that 200 nm $\approx$ R$_P$ + 3ΔR$_P$. This shows that damage creation process in 6H-SiC is extremely efficient when the implantation is done at room temperature. This also

indicates that xenon is fixed firmly into the amorphous region. The depth of the amorphous layer is measured as the depth between the half maximum of Si surface signal and half maximum of the Si signal as it decreases at the end of the amorphous layer. Thus the, 6H-SiC implanted at room temperature has an amorphous region and crystalline region.

6H-SiC retained its crystallinity after implantation at 600 ^{o}C with damage in the implanted region due to the defects introduced by the implantation. The damage is indicated by the broad peak around 150 nm. The projected range predicted by SRIM is R_P =101 nm, while the experimental is R_p=113 nm. The discrepancy is explained in 6.1.2 below. The damage to average depth of about R_P =113 nm corresponds to the maximum ion concentration, the deviation of range due to energy straggling is ΔR_P =35.3 nm. Comparing the depth with the typical projected range R_p and the range straggling of ΔR_p, it follows that 150nm $\approx R_p + \Delta R_P$.

The difference in the radiation damage retained after implantations is caused by the difference in the implantation temperatures. Implanting Xe ions with the same energy at different temperatures into 6H-SiC displaces both Si and C atoms, the displaced atoms at higher temperature would have more energy to move around, increasing the probability of the displaced atoms to recombine with their original lattice sites. Similar radiation hardness was reported for other heavy implanted ions at temperatures above 300 ^{o}C by Hlatswayo et al [Hla12], Wendler et al [Wen98] and by Fukuda et al [Fuk76].
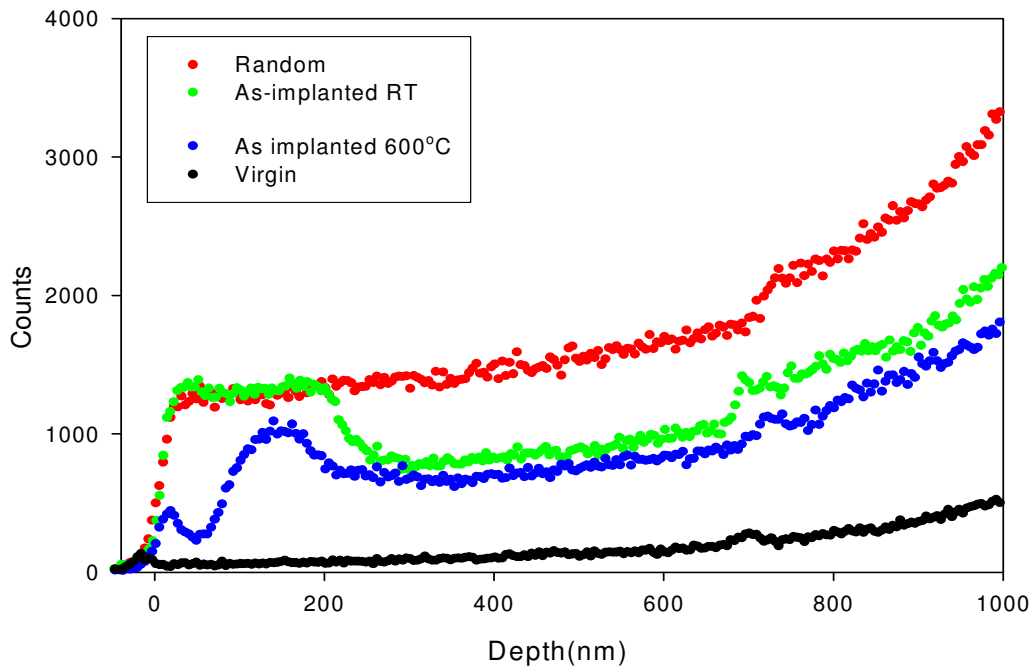
Figure 6-2: Random and aligned RBS spectra of 6H-SiC implanted at 23 ^{o}C and 600 ^{o}C with 360 keV $^{133}Xe^+$ to a fluence of 1 × 10^{16} cm^{-2}. Also shown is the aligned spectra of the unimplanted 6H-SiC. The α-particle energy was 1.6 MeV and the scattering angle was 165°.

Figure 6-3 shows that the depth profile of the damage created during implantation (damage peak on Si) by the xenon ions nearly corresponds to implanted xenon distribution profile. This confirms that xenon is embedded inside 6H-SiC at a depth of about 150nm. Damage profile is slightly deeper due to the knock-on effect of the heavier bombarding Xe on the lighter substrate atoms, displacing them deeper inside the substrate into interstitial positions.
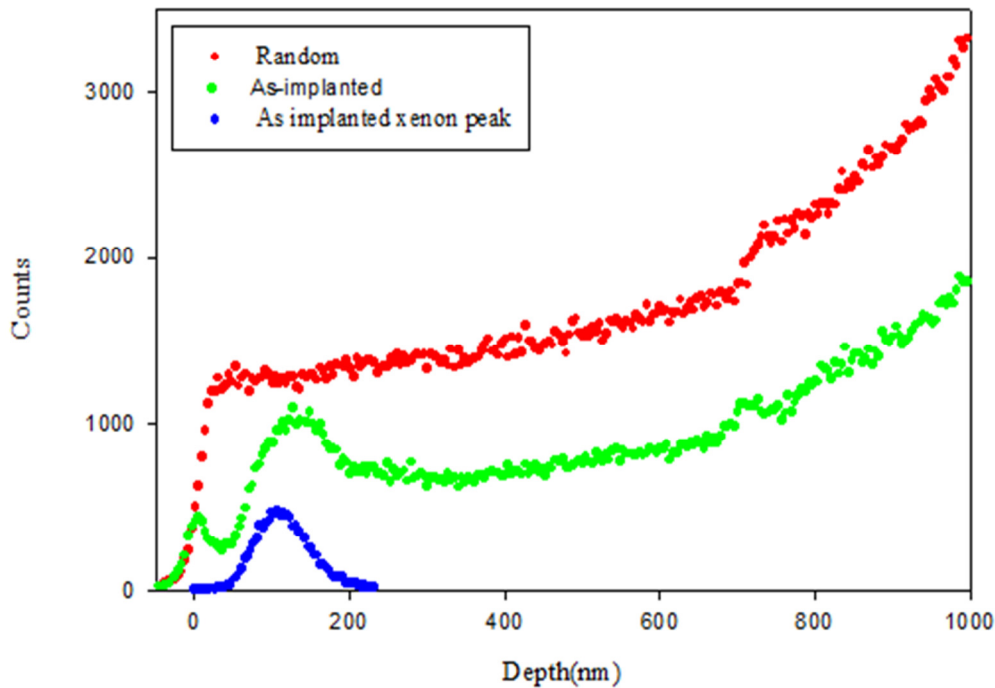
Figure 6-3: The random and aligned Rutherford backscattering spectrum of 6H-SiC implanted at 600 ^{o}C compared with the as-implanted xenon profile peak.

The 600 ^{o}C implanted samples were isochronally annealed at temperatures ranging from 1000 ^{o}C to 1500 ^{o}C for 5h in steps of 100 ^{o}C. The results are depicted in figure 6-4. The initial annealing of the sample at 1000 ^{o}C showed that a small amount of defects were removed. This was indicated by the reduction in height of the damage peak. At 1100 ^{o}C a further defects were removed in comparison to 1000 ^{o}C. A great amount of defects were removed at 1200 ^{o}C when comparing it to the as implanted. The damage removed at 1200° C was high when taking 1100 ^{o}C as a reference point.

Most radiation damage was retained at lower annealing temperatures (i.e. T_a < 1200 ^{o}C) because the defects probably annealed into dislocation loops which are hard to anneal out. Annealing at 1300 ^{o}C further annealed defects left after 1200 ^{o}C annealing. At 1400 ^{o}C a great amount of radiation damage was annealed out. As the temperature increases the greater the energy of the substrate atoms thereby increase their mobility and the probability of the displaced atoms to combine with their original lattice sites. At 1500 ^{o}C the damage peak has almost disappeared, but

58

the virgin spectrum was not achieved. This happened because of dechanneling due to exte̶n̶d̶e̶d̶ ̶d̶e̶f̶e̶c̶t̶s̶ ̶l̶i̶k̶e̶ ̶d̶i̶s̶l̶o̶c̶a̶t̶i̶o̶n̶s̶
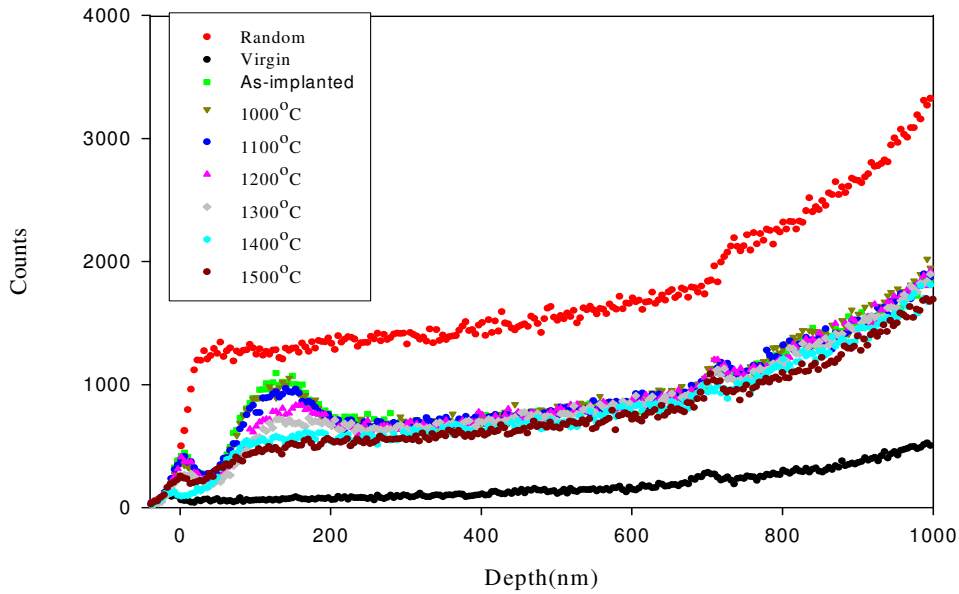

Figure 6-4: The random and aligned Rutherford backscattering spectra of 6H-SiC spectra implanted at 600 ᵒC and submitted to isochronal annealing of 5h.

6.2 Diffusion Results

6.2.1 As-implanted xenon profiles

The Xe RBS depth profiles of xenon implanted at 23 ^{o}C and 600 ^{o}C as compared SRIM12 simulation are shown in figure 6-5. The experimental data were fitted on the Edgeworth distribution using GENPLOT fitting computer program to obtain the four moments of xenon distribution function i.e. Projected range (R_p), standard deviation ($\Delta R_p/\sigma$), Kurtosis (β), and skewness (γ) . The mathematical formula showing the moments mentioned above are written as follows:

$$R_P = \frac{\sum_i x_i}{N}, \sigma = \left[\frac{\sum_i x_i - R_P}{N}\right]^{\frac{1}{2}}, \gamma = \frac{\sum_i (x_i - R_P)^3}{N\sigma^3} \ and \ \beta = \frac{\sum_i (x_i - R_P)^4}{N\sigma^4}$$

Where x_i is the distance from the surface to the implanted ions and N is the number of implanted ions. A Gaussian distribution has $\gamma = 0$ and $\beta = 3$. The Edgeworth distribution is written as follows [Hla10]:

$$f(x) = g(x)p(x)$$

where

$$g(x) = \frac{h}{\sqrt{2\pi}} \exp\left(\frac{-\arg(x)}{2}\right)$$

and

$$p(x) = 1 + \frac{\gamma\,(arg\,x)^3 - 3\,arg(x)}{6} + \frac{(\beta - 3)(arg\,x)^4 - 6\,(arg\,x)^2 + 3)}{24}$$

with

$$arg(x) = \frac{(x - R_P)}{\sigma}$$

and where *h* is the height fitting parameter.

The experimental and SRIM12 moments are shown in Table 1. The projected ranges of 360 keV xenon ions implanted at 23 ^{o}C and 600 ^{o}C are essentially equal to each other but are about 10% larger than the predicted value by SRIM12. The projected range straggling ΔR_P of both the 23 ^{o}C and 600 ^{o}C implantations are slightly larger as compared to the SRIM12 prediction, although the concentration is the same for all peaks. The skewness and kurtosis of the implanted profiles differ by almost 50% to that of SRIM12 predictions. These differences are caused by the fact that SRIM12 makes a number of approximations in simulating the interactions between the bombarding ions and the substrate atoms. The most important of these approximations include:

- The substrate is amorphous. Thus, SRIM does not take any crystallinity effects into account.
- Only binary collisions are considered in SRIM12. Thus, the influence of neighboring atoms is neglected. Spike bombardment effects are consequently also neglected.
- The recombination of knocked out atoms with the vacancies is neglected.
- The electronic stopping is an averaging fit to a large number of experiments.

Comparing the Xe RBS spectra of 600 ^{o}C implantation with the 23 ^{o}C implantation, broadening of the peak at 600 ^{o}C is observed. This means that a slight diffusion was already taking place during 600 ^{o}C implantation. This diffusion is due to irradiation induced diffusion, is shown by the change in ΔRp (broadening) and the reduction of the xenon peak area. Friedland et al. [Fri11] also reported similar diffusion behaviour

when silver and iodine where implanted in 6H-SiC. The skewness of 23 ^{o}C and 600 ^{o}C is positive as can be seen in figure 6-5 that it tails towards the bulk.

Table 1: *The first four moments obtained from GENPLOT [www1] by fitting experimental values to the Edgeworth distribution, and from SRIM12 [Zie77].*

	23 ^{o}C	600 ^{o}C	SRIM12
R$_p$ (nm)	112.4	113.0	101
ΔR$_p$ (nm)	28.7	35.3	24.0
Skewness (γ)	0.24	0.56	0.12
Kurtosis (β)	2.70	3.01	2.83

The as-implanted xenon profiles can be described as nearly Gaussian distribution from the moments given in table 1. For a perfectly Gaussian profile γ=0 and β=3, values smaller or larger than this make the profile to be asymmetric [Suz10]. R$_p$ indicates the average depth of the xenon ion concentration and ΔR$_p$ shows the degree of spread in the R$_p$ profile.
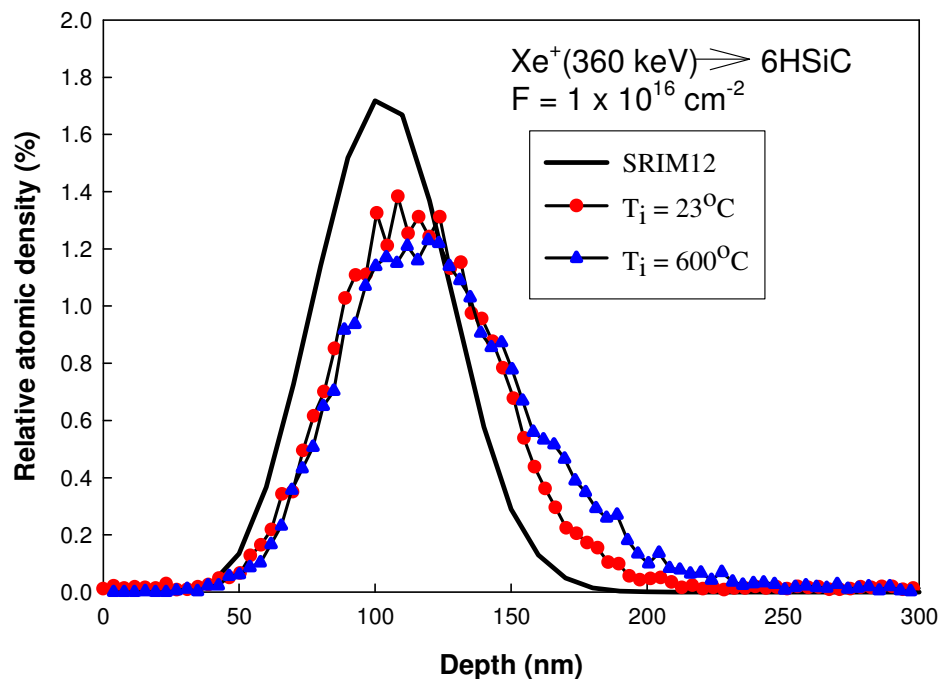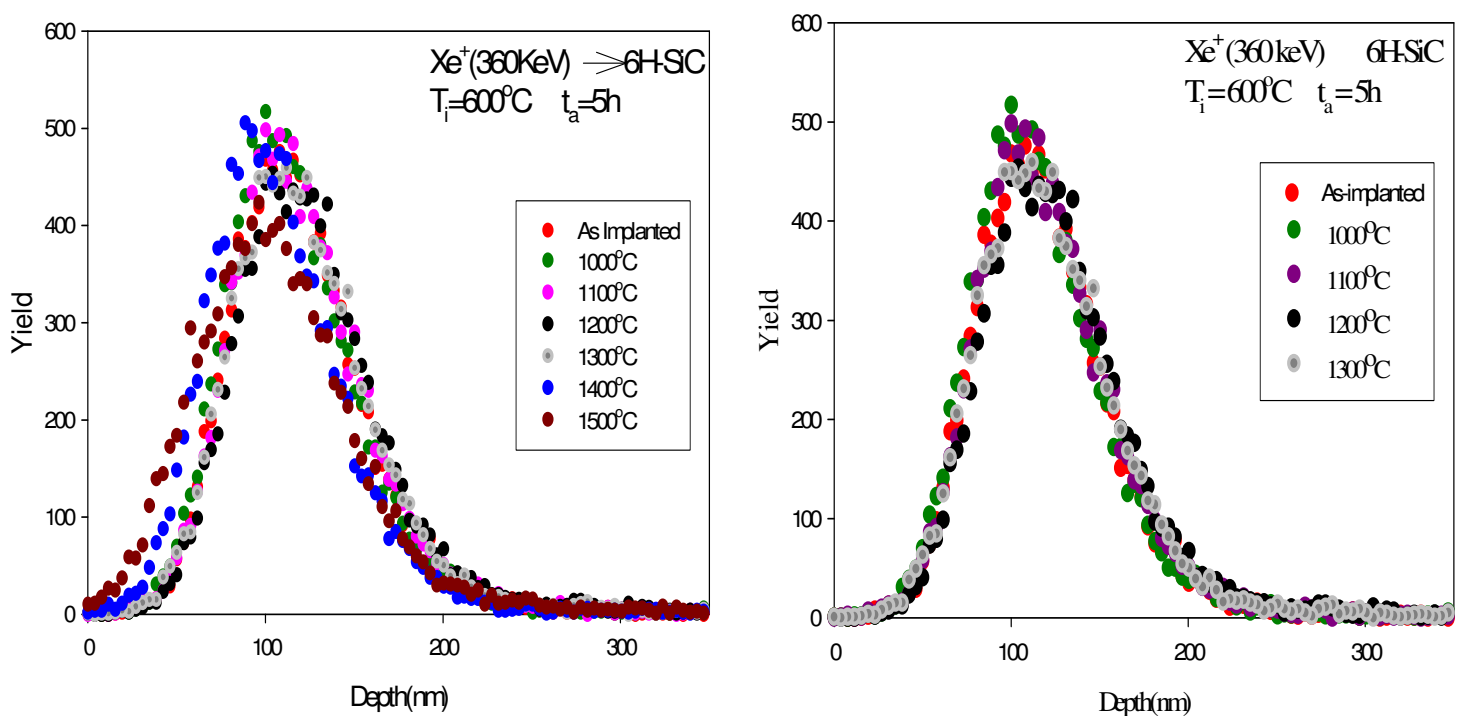

Figure 6-5: *Xenon profile in 6H-SiC implanted at 23 ^{o}C and 600 ^{o}C compared to SRIM12 prediction.*

6.2.2 **Isochronal annealing results**

The diffusion of Xe was investigated by annealing the samples at temperatures ranging from 1000 ^{o}C to 1500 ^{o}C in steps of 100 ^{o}C. The square of the full width at half maximum as the function of annealing temperature was plotted to study the diffusion behavior of xenon. The R_P as a function of annealing temperature was plotted to study the shift of the xenon profile. Finally, the retained ratio as a function of annealing temperature was plotted to investigate the retainment of the implanted xenon.

6-6: *Xenon depth profile in 6H-SiC implanted at 600 ^{o}C after isochronal annealing.*

The isochronal annealing depth profile results are shown in Figure 6-6 and 6-7. As-implanted spectrum is used as the point of reference. When the sample was annealed at 1000 ^{o}C and 1100 ^{o}C, the xenon profile remained the same. Annealing further at 1200 ^{o}C and 1300 ^{o}C showed no significant change in the xenon profile. A shift of the profile towards the surface took place when the sample was annealed at 1400 ^{o}C. Further shift towards the surface at 1500 ^{o}C also took place. This shift towards the

62

surface can be explained to be due to thermal etching. Hlatshwayo et al. [Hla12] studied the diffusion behavior of Ag^+ implanted into 6H-SiC at 350 ^{o}C and 600 ^{o}C using RBS, scanning electron microscopy (SEM) and Raman for analysis. At 1500 ^{o}C they noticed a shift of the silver profile towards the surface in their RBS results. They did SEM to check the cause of the shift, which was said to be due to thermal etching of SiC [Van12]. The shift at 1500 ^{o}C is accompanied by diffusion. This type of diffusion taking place is volume diffusion. Fukuda et al. [Fuk76] studied Xe in pyrolytic SiC using γ-ray spectrometry; they explained the release of xenon above 1400 ^{o}C due to normal volume diffusion without hindrance of trapping effect.
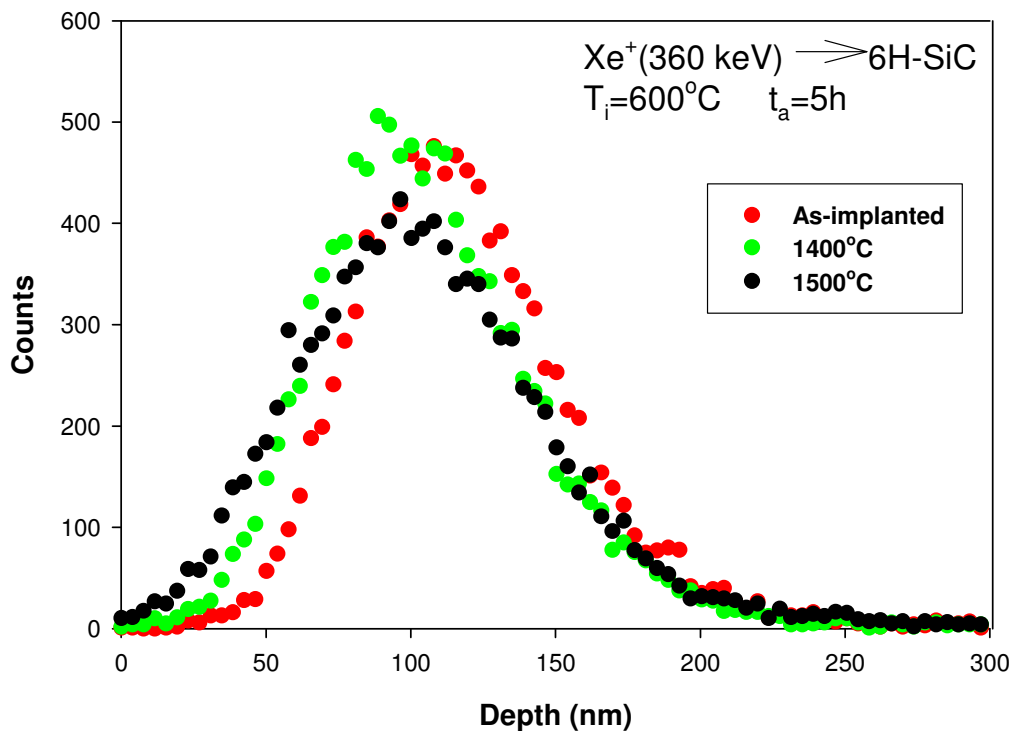

Figure 6-7: The Xenon depth profile of the as-implanted, 1400 ^{o}C and 1500 ^{o}C spectra isochronally annealed for 5h.

From the brief discussion above it follows that Fick's diffusion discussed in section 2.2 is probably not the main diffusion mechanism taking place in SiC in the total temperature range studied in this dissertation – it is only valid above 1400 ^{o}C. At the lower temperatures, it is defect-trap related diffusion. In our case during implantation

63

a lot of defects are introduce to the SiC material. As will be shown and discussed at the end of this section, when we anneal we do not get rid of the implanted species. The defects capture the impurities and when the sample is annealed the defects are broken up and they release the impurities, and the impurity will again be captured by another defect. This process transforms to a stable defect.
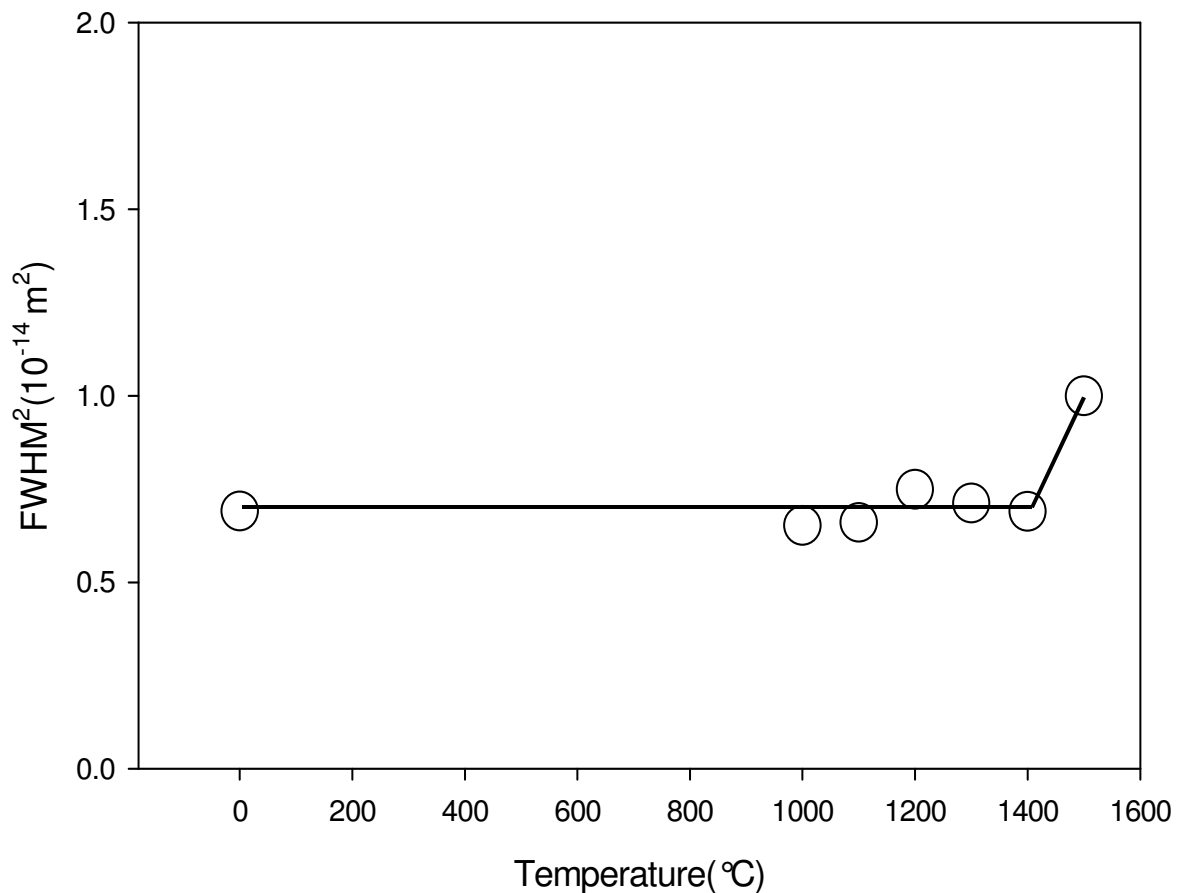

Figure 6-8: Square of the full width at half maximum of xenon in 6H-SiC as a function of temperature.

The experimental RBS profiles for the Xe peak in the annealed spectra were also fitted to the GENPLOT computer program to obtain the FWHM and projected range R_P values. Figure 6-8 shows the $FWHM^2$ as a function of temperature. The FWHM indicates whether there is broadening of the peak, which is shown by an increase in the FWHM. In Figure 6-8 the $FWHM^2$ remains the same with the increase in temperatures (from 1000 to 1400 ^{o}C) as compared to the as implanted. From the graph we can deduce that no diffusion takes place at these annealing temperatures. This

64

agrees with the RBS xenon profile from figure 6.6 and 6.7 above. At 1500 $^{\circ}$C the FWHM[2] increases. This indicates that at this annealing temperature diffusion is taking place.
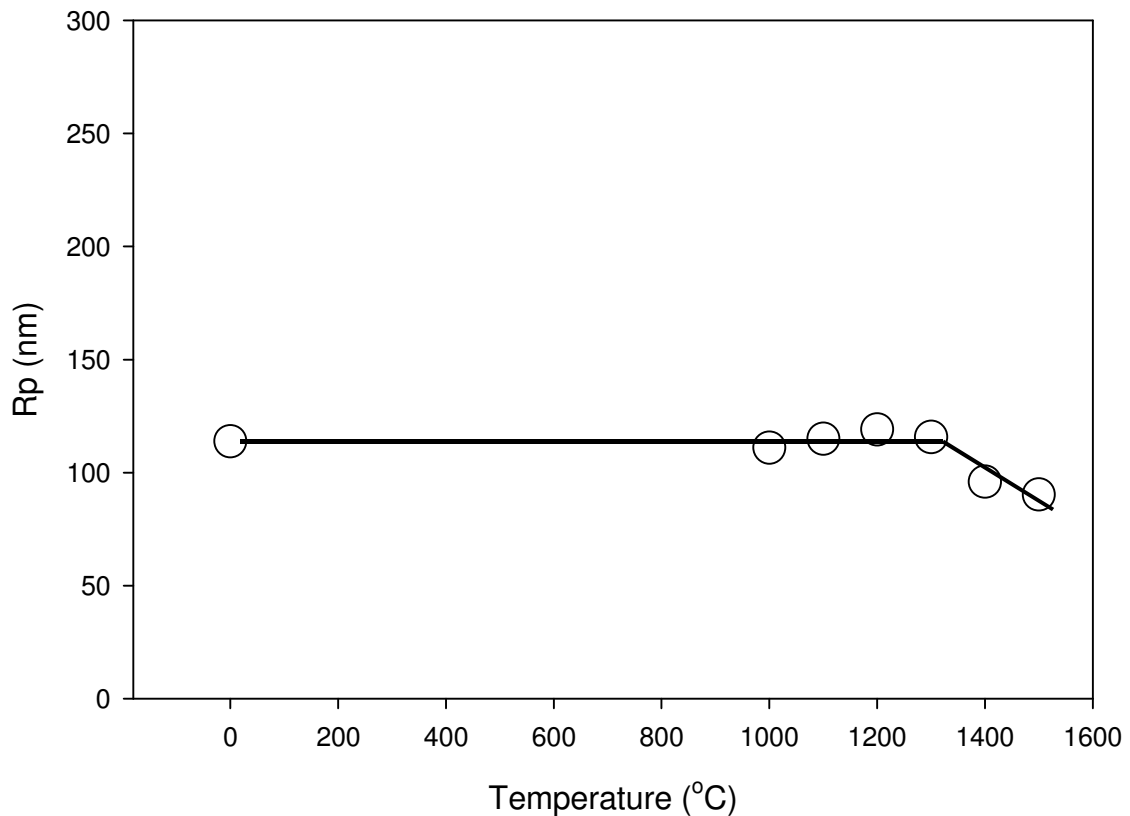

Figure 6-9: Projected range of xenon at different temperatures as a function of temperature.

Figure 6-9 shows the R_p as the function of temperature. The R_p graph agrees with the xenon profile graph. The projected range of the annealing temperatures 1000 to 1300 $^{\circ}$C as compared to the as-implanted remains the same. A change in R_p (that is a decrease) takes place at 1400 $^{\circ}$C and further decreases at 1500 $^{\circ}$C. The decrease indicates a shift of the xenon profile towards the surface which is due to that thermal etching. This etching does not affect the implanted xenon profile behavior and the diffusion taking place at 1500 $^{\circ}$C.

Figure 6-10 depicts the retained ratio as a function of temperature. By retained ratio we mean the amount of implanted profile which is left after annealing as compared

with the initial implantation quantity. From the graph it is evident that no xenon is lost, all of the implanted xenon is retained in the 6H-SiC substrate. This indicates that the thermal etching does not affect the storage and diffusion behavior of xenon profile at these annealing temperatures.
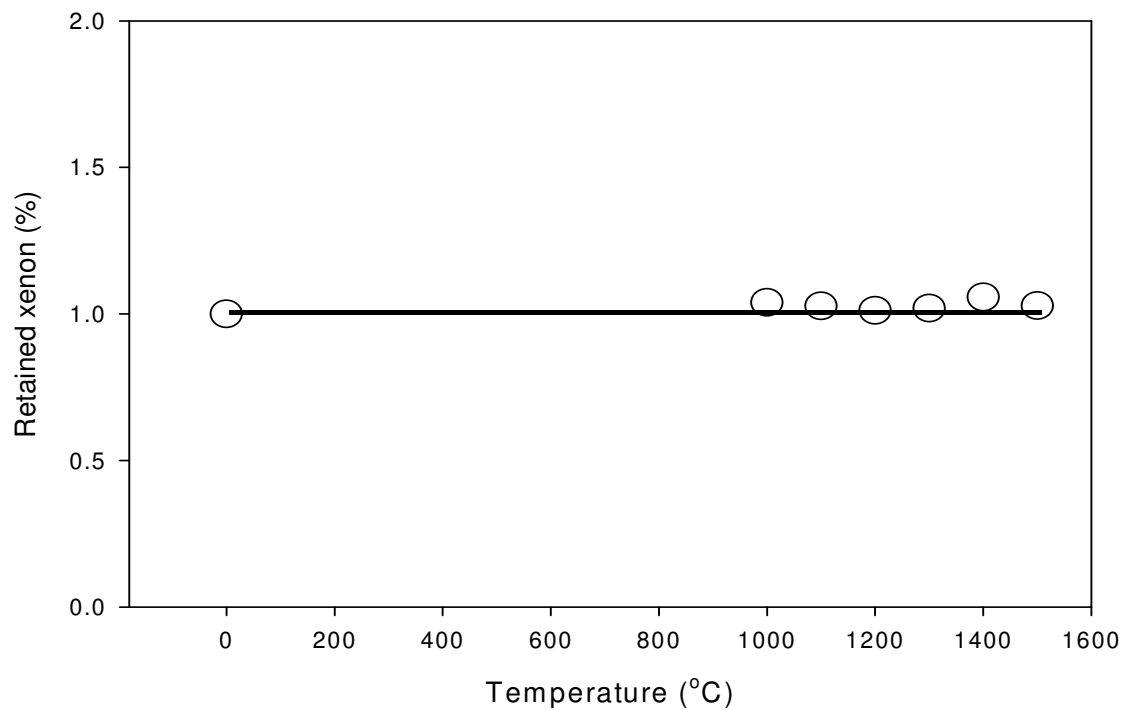

Figure 6-10: The ratio of the retained xenon in 6H-SiC after isochronal annealing.

6.3 References

[Fri11]   E. Friedland, N. G. van der Berg, J. B. Malherbe, J.J. Barry, E. Wendler and W. Wesch, J. Nucl. Mater. 410 (2011) 24.

[FuK76] K. Fukuda and K. Iwamoto, J. Mater. Sci. 11 (1976) 522.

[Hla10] T. T. Hlatshwayo," Diffusion of silver in 6H-SiC", PhD Thesis, Department of Physics, University of Pretoria, (2010).

[Hla12] T.T. Hlatshwayo, J.B. Malherbe, N.G. van der Berg, A,J. Botha and P. Chakraborty, Nucl. Instr. Meth. Phys. B 273 (2012) 61.

[Suz10] K. Suzuki, FUJITSU Sci. Tech. J. 46 (2010) 307.

[Van12] N.G. van der Berg, J.B. Malherbe, A.J. Botha and E. Friedland, Appl. Surf. Sci, 258 (2012) 5561

[Wen98] E. Wendler , A. Heft and W. Wesch, Nucl. Instr. Meth. Phys. B 141 (1998) 105.

[www1] www.genplot.com, 6 June 2012.

[Zie77] J. F. Ziegler, J. P. Biersack and U. Littmark, "The Stopping Power and Range of Ions in Matter", vol. 1-6, Pergamon Press, New York ,(1977- 85).

CHAPTER 7

CONCLUSIONS

In this study the diffusion of xenon implanted into 6H-SiC at 600 ^{o}C and annealing of the radiation damage were investigated at temperatures ranging from 1000 ^{o}C to 1500 ^{o}C in steps of 100 ^{o}C using RBS and RBS-C. The implantation temperature of 600 ^{o}C was used to approximately simulate reactor conditions. RBS and RBS-C results indicated that the 6H-SiC retained its crystallinity with some damage in the implanted region (depth of about 150nm) due to the defects introduced by the implantation. This is because of the fact that at 600 ^{o}C implantation the displaced atoms were mobile due to the high energy they possessed. This indicated the radiation hardness of 6H-SiC during implantation. RBS and RBS-C analysis of the isochronally annealed sample (from 1000 to 1400 ^{o}C in steps of 100 ^{o}C) indicated the removal of the damage to be taking place. As the annealing temperature increases the greater the energy of the substrate atoms thereby increase their mobility and the probability of the displaced atoms to combine with their original lattice site. At 1500° C the damage peak had almost disappeared, but the virgin spectrum was not achieved. This happened because of dechanneling due to extended defects like dislocations.

Slight diffusion during implantation took place and this diffusion is due to irradiation induced diffusion. No diffusion was observed during annealing at temperatures from 1000 to 1400 ^{o}C. However, the shift of the profile towards the surface was observed from1400 ^{o}C to1500 ^{o}C. This was due to thermal etching of SiC. The profile shift at 1500° C was accompanied by volume diffusion. From our results it was evident that no xenon was lost, all of the implanted xenon was retained in the 6H-SiC substrate. This proves that the thermal etching did not affect the retainment and diffusion behaviour of xenon profile at temperatures of annealing.

Modern high temperature gas-cooled reactors operate at temperatures above 600 ^{o}C in the range of 750 ^{o}C to 950 ^{o}C. Consequently, our results indicate that the volume diffusion of Xenon in SiC is not significant in SiC coated fuel particles.

For future work further investigation needs to be carried out so as to be able to calculate the diffusion coefficient and activation energy of xenon implanted in 6H-SiC by doing isothermal annealing. We also plan to investigate samples implanted at different temperatures like (room temperature, 350 and 600 $^{\circ}$C) and to use different techniques such as Scanning electron microscopy (SEM), Raman spectroscopy, X-ray Diffraction (XRD) and Transmission electron microscopy (TEM) in order to gain a better understanding of the mechanisms occurring in the samples during implantation and the subsequent annealing. This work reported here was also presented in the following conferences:

1. South African Institute of Physics conference held 9-13th July 2012 at University of Pretoria in South Africa - Poster presentation.

2. South African Institute of Physics conference held 8-12th July 2013 at University of Zululand (Richards Bay) in South Africa - Oral presentation.

3. Ion-Surface Interactions conference held 22- 26th August 2013 at Yaroslavl in Russia - Poster presentation.

A summary of our findings were also reported as an extended abstract in the proceedings of the Ion-Surface Interactions conference held 22- 26th August 2013 at Yaroslavl in Russia.